

Chapter 2

Photoionization and Interatomic Coulombic Decay

The type of process that may be induced in an atom by the interaction with a single photon is strongly dependent on the photon energy. An overview of the energy regimes in the electromagnetic spectrum is given in Fig. 2.1. For wavelengths in the infrared (IR) and optical regime, electron-photon interaction is dominated by elastic Rayleigh scattering. For ultraviolet (UV) radiation and X-rays up to a few keV, inelastic photoabsorption is the most relevant process. For even higher photon energies, Compton scattering becomes dominant and is eventually taken over by pair creation when the energy increases further. Throughout this thesis we will mostly address the interaction of extreme ultraviolet radiation (XUV), corresponding to the energy regime of $10 \text{ eV} < h\nu < 124 \text{ eV}$, with atoms and molecules, which usually leads to photoionization.

The absorption of a single and of multiple photons in a one-electron system is introduced in Sect. 2.1. For the description of a system consisting of more than just a core and an electron, the electron-electron interaction must be taken into account. Common techniques and approximations used to describe the Coulomb repulsion between the electrons and the electron correlation for atoms and molecules are presented in Sect. 2.2. The cross sections for the absorption of single XUV photons are discussed in Sect. 2.3. As high energetic photons efficiently remove inner-shell and core electrons, highly excited ions are often created. The most relevant relaxation mechanisms are explained in Sect. 2.4. One particular relaxation mechanism, interatomic Coulombic decay (ICD), which relies on the Coulomb interaction of a highly excited monomer with its environment, is presented in Sect. 2.5. A classical simulation for pump-probe schemes, which is applied to extract time-information for such molecular processes, is presented in Sect. 2.6. The chapter concludes with a model for charge transfer in dissociating molecules in Sect. 2.7.

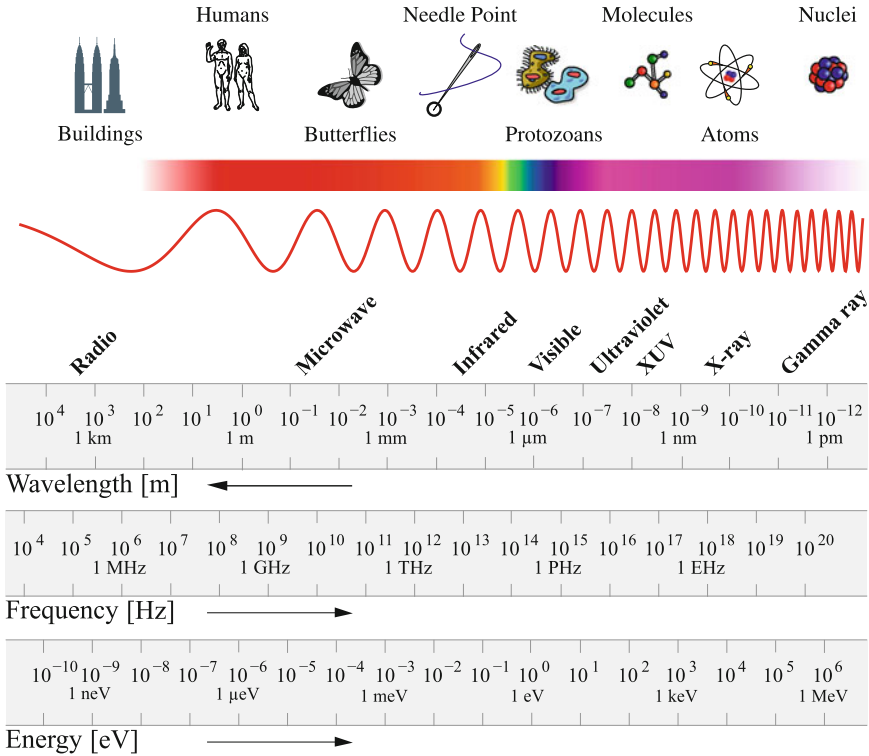


Fig. 2.1 Electromagnetic spectrum. Adapted from [79, 80]

2.1 Photon-Atom Interaction

The response of atoms to electromagnetic radiation depends on the wavelength and the field strength. While weak fields may be treated perturbatively, strong fields require a different approach. These two regimes will be discussed in the following section, starting with the weak field in Sect. 2.1.1. Following this, the transition from weak to strong fields is discussed in Sect. 2.1.2.

2.1.1 Single- and Multi-photon Absorption

We start by giving a short introduction to the quantum mechanical treatment of a hydrogen-like atom interacting with an electromagnetic wave. The following considerations are compiled from [29, 38, 44]. Please note, that the equations are given in atomic units. For further details on the applied unit system see Appendix.

The interaction of an atom with a classical field is described by introducing the minimal coupling $\mathbf{p} \rightarrow \mathbf{p} - \mathbf{A}/c$ into the non-relativistic Hamiltonian:

$$\hat{H} = \frac{1}{2} \left(\mathbf{p} - \frac{\mathbf{A}}{c} \right)^2 + V(r). \quad (2.1)$$

Here, \mathbf{p} is the momentum operator, \mathbf{A} is the vector potential of the electromagnetic field in Coulomb gauge $\nabla \cdot \mathbf{A} = 0$, and $V(r) = -Z/r$ is the Coulomb potential for an electron in the field of a nucleus with charge Z . The \mathbf{A}^2 term is neglected as we assume the electromagnetic field to be weak. The full Hamiltonian from Eq. (2.1) is separated into the Hamiltonian of a free atom $\hat{H}_0 = \mathbf{p}^2/2 - Z/r$ and the interaction term $\hat{H}_{\text{int}} = -\mathbf{p} \cdot \mathbf{A}/c$, describing the coupling to the external field. Here, we made use of $\mathbf{p} \cdot \mathbf{A} = \mathbf{A} \cdot \mathbf{p}$. The time evolution of the system is governed by the time-dependent Schrödinger equation

$$i \frac{\partial}{\partial t} \Psi(\mathbf{r}, t) = \hat{H} \Psi(\mathbf{r}, t) = (\hat{H}_0 + \hat{H}_{\text{int}}) \Psi(\mathbf{r}, t). \quad (2.2)$$

If the interaction term is weak, Eq. (2.2) can be solved using time-dependent perturbation theory. In order to do so we introduce the parameter λ , which will denote the order of perturbation theory:

$$i \frac{\partial}{\partial t} \Psi(\mathbf{r}, t) = (\hat{H}_0 + \lambda \hat{H}_{\text{int}}) \Psi(\mathbf{r}, t). \quad (2.3)$$

The unperturbed Hamiltonian \hat{H}_0 is not anymore the exact Hamiltonian of the system. Its known eigenfunctions $\psi_k(\mathbf{r})$ form a complete basis set. Therefore, the full solution of the Schrödinger equation may be expanded in this basis with the time-dependent expansion coefficients $c_k(t)$:

$$\Psi(\mathbf{r}, t) = \sum_k c_k(t) \psi_k(\mathbf{r}) e^{-iE_k t}. \quad (2.4)$$

Upon insertion of this expansion into Eq. (2.3), a system of coupled differential equations enumerated by b , is obtained:

$$\frac{\partial c_b(t)}{\partial t} = \frac{1}{i} \sum_k \lambda c_k(t) \langle \psi_b | \hat{H}_{\text{int}} | \psi_k \rangle e^{i(E_b - E_k)t}. \quad (2.5)$$

This system may be solved by using a perturbative approach, if $\lambda \hat{H}_{\text{int}}$ is small. The coefficients c_k are expanded in powers of the parameter λ :

$$c_k(t) = c_k^{(0)}(t) + \lambda c_k^{(1)}(t) + \lambda^2 c_k^{(2)}(t) + \dots \quad (2.6)$$

The expansion from Eq. (2.6) is then inserted into Eq. (2.5) and the solutions of the individual orders are found iteratively by integration in time. At time $t = 0$ the system is prepared in its initial state ψ_a , which has to be ensured by the zeroth order of the expansion series, thus $c_k^{(0)} = \delta_{ka}$. In order to calculate the next higher order term the resulting coefficient from the previous order is inserted into Eq. (2.5) and integrated in time. Exemplary, the first- and second-order terms in λ are given in the following. They describe a single or a double interaction with the electromagnetic field, leading to the transition of the system from the initial state ψ_a to a final state ψ_b .

$$\lambda^0 : c_b^{(0)}(t) = \delta_{ba} \quad (2.7)$$

$$\lambda^1 : c_b^{(1)}(t) = \frac{1}{i} \int_0^t dt' \langle \psi_b | \hat{H}_{\text{int}}(t') | \psi_a \rangle e^{i(E_b - E_a)t'} \quad (2.8)$$

$$\begin{aligned} \lambda^2 : c_b^{(2)}(t) = & \frac{1}{i^2} \sum_k \int_0^t dt' \int_0^{t'} dt'' \langle \psi_b | \hat{H}_{\text{int}}(t') | \psi_k \rangle \langle \psi_k | \hat{H}_{\text{int}}(t'') | \psi_a \rangle \\ & \times e^{i(E_b - E_k)t'} e^{i(E_k - E_a)t''} \end{aligned} \quad (2.9)$$

The contribution of the electromagnetic field is expressed by the interaction Hamiltonian $\hat{H}_{\text{int}} = -\mathbf{p}\mathbf{A}/c$. The vector potential is assumed to be a plane wave

$$\mathbf{A}(\mathbf{r}, t) = A_0 \mathbf{e}_{\text{pol}} \left(e^{i(\mathbf{k}\mathbf{r} - \omega t)} + e^{-i(\mathbf{k}\mathbf{r} - \omega t)} \right), \quad (2.10)$$

where \mathbf{e}_{pol} is a unit vector in polarization direction and \mathbf{k} is the wave vector with $|\mathbf{k}| = 2\pi/\lambda$. If the wavelength of the electromagnetic wave λ is large compared to the dimensions of an atom, $\mathbf{k}\mathbf{r} \ll 1$, the dipole approximation $e^{i\mathbf{k}\mathbf{r}} \approx 1$ is applicable. This assumption is justified up to photon energies of a few kiloelectronvolt and is thus also valid for the XUV regime.

Then, the interaction Hamiltonian can be rewritten as $\hat{H}_{\text{int}} = -\mathbf{d}\boldsymbol{\epsilon}$ using the electric field $\boldsymbol{\epsilon} = -\frac{1}{c} \frac{\partial \mathbf{A}}{\partial t}$ and the dipole operator $\mathbf{d} = q\mathbf{r}$. According to our applied unit system, we set the charge $q = e = 1$. An instructive derivation of this transformation may be found in [23], using the kinetic momentum $\mathbf{p} = \frac{\partial \mathbf{r}}{\partial t}$:

$$\hat{H}_{\text{int}} = -\frac{1}{c} \mathbf{p}\mathbf{A} = -\frac{1}{c} \frac{\partial \mathbf{r}}{\partial t} \mathbf{A} = \mathbf{r} \underbrace{\frac{1}{c} \frac{\partial \mathbf{A}}{\partial t}}_{-\boldsymbol{\epsilon}} - \underbrace{\frac{1}{c} \frac{\partial}{\partial t} (\mathbf{r}\mathbf{A})}_0, \quad (2.11)$$

where the latter term vanishes due to the Coulomb gauge. For an exact derivation, which is also valid beyond the dipole approximation, the so-called Power-Zienau-Woolley transformation must be performed [59, 82].

For an electromagnetic field polarized in x -direction and the absorption¹ of photons this leads to

$$\hat{H}_{\text{int}} = x \epsilon_0 e^{-i\omega t}. \quad (2.12)$$

Inserting this \hat{H}_{int} into Eqs. (2.8) and (2.9) yields the first and second order expansion coefficients, respectively. Particularly, the integrations in time may be performed using a representation of Dirac's δ -function:

$$\delta(x) = \frac{1}{2\pi} \int_0^\infty dt e^{ixt}. \quad (2.13)$$

The probability for finding the system in the eigenstate ψ_b , due to n -photon absorption, after a certain time t is given by

$$w_{a \rightarrow b}^{(n)}(t) = \left| c_b^{(n)}(t) \right|^2. \quad (2.14)$$

Assuming that the transition is induced by a laser with intensity $I_0 \propto \epsilon_0^2$, which is turned on for a duration τ , the transition rate is given by

$$R_{a \rightarrow b}^{(n)} = \frac{w_{a \rightarrow b}^{(n)}(\tau)}{\tau}. \quad (2.15)$$

Note that, the squared δ -function in $w_{a \rightarrow b}^{(n)}$ leads to a factor containing the duration τ [8], which cancels with the $1/\tau$ in $R_{a \rightarrow b}^{(n)}$. Thus, the rate for the first and second order process reads:

$$R_{a \rightarrow b}^{(1)} \propto I_0 |\langle \psi_b | x | \psi_a \rangle|^2 \delta(E_b - E_a - \omega), \quad (2.16)$$

$$R_{a \rightarrow b}^{(2)} \propto I_0^2 \sum_k \langle \psi_b | x | \psi_k \rangle \langle \psi_k | x | \psi_a \rangle \delta(E_b - E_a - 2\omega). \quad (2.17)$$

The intuitive picture for the two-photon absorption process is that an electron is excited from the initial state ψ_a to an intermediate state ψ_k by the first photon and from the intermediate state to the final state ψ_b by the second photon [33]. Note that the intermediate state is virtual, i.e., not necessarily an eigenstate of the atom.

So far, we found that the transition rate for the single-photon absorption grows linearly in the laser intensity, while the two-photon case grows squared. Continuing our consideration to the absorption of n photons, by taking the respective orders in the perturbative expansion from Eq. (2.6), shows

¹ Had we chosen the negative exponent of Eq. (2.10), $e^{-i(\mathbf{k}\mathbf{r}-\omega t)}$, stimulated emission instead of photon absorption would be described.

$$R_{a \rightarrow b}^{(n)} \propto I_0^n. \quad (2.18)$$

Although the previous derivations were only made for a transition between two bound states, the same behavior is found for a final state in the continuum. Thus, the result is also applicable for photoionization [29].

It is important to stress that we observe two different mechanisms of multi-photon absorption in the experiment, sequential and direct photon absorption. The I_0^n -scaling found in this section is valid for the direct case. There, the intermediate states are virtual and their—usually short—lifetime is determined by Heisenberg's uncertainty relation. Thus, the photon absorption must occur directly within the limited lifetime of the state, i.e., quasi simultaneously.

In the sequential case, the first photon ionizes the system, another photon ionizes the created ion and so forth. This process can be described as a sequence of single-photon absorptions, which may occur at any time during the pulse. Thus, all populated intermediate states are stationary and the probability to absorb another photon is linearly dependent on the intensity and the number of available ions.

2.1.2 Atoms in Strong Laser Fields

The motion of an atom in a laser field $\epsilon = \epsilon_0 \cos \omega t$ can be simplified by assuming that a single electron oscillates in an electromagnetic field, while the much heavier core remains fixed. Classically, the electron's oscillation is described via Newton's *lex secunda*, as described in [38]:

$$m_e \frac{dv}{dt} = e\epsilon \rightarrow v = \frac{e\epsilon_0}{m_e\omega} \sin \omega t \quad (2.19)$$

with a kinetic energy of

$$\frac{1}{2} m_e v^2 = \frac{e^2 \epsilon_0^2}{2 m_e \omega^2} \sin^2 \omega t. \quad (2.20)$$

The average of Eq. (2.20) over one laser period is the so-called ponderomotive potential U_p , which is interpreted as the energy of an electron that performs a quiver motion in the oscillating electric field of the laser. It is given by

$$U_p = \frac{1}{2} m_e \langle v^2 \rangle = \frac{e^2 \epsilon_0^2}{4 m_e \omega^2} = \frac{e^2}{8 \pi^2 \epsilon_0 c^3 m_e} I_0 \lambda^2. \quad (2.21)$$

A comparison of U_p for ionization with an IR and an equally intense XUV pulse is given in Table 2.1. While the ponderomotive potential of an electron in the XUV field is completely negligible, it is already two times larger than the electron's binding energy in I_2 for the IR pulse. Therefore, the influence of the XUV pulse may be

Table 2.1 Ionization of I_2 with an ionization potential $E_I = 10 \text{ eV}$ via an IR pulse of $3.4 \times 10^{14} \frac{\text{W}}{\text{cm}^2}$ and an XUV pulse with the same intensity. The Keldysh parameter γ and the ponderomotive potential U_p are given

	$\lambda \text{ (nm)}$	γ	$U_p \text{ (eV)}$
IR	800	0.5	20
XUV	14	84	<0.001

treated as a weak perturbation. In contrast, the IR field is strong enough to deform the potential.

The ionization of atoms in strong laser fields is described within two different pictures, which one applies is characterized by the so-called Keldysh parameter [42]

$$\gamma = \sqrt{\frac{E_I}{2U_p}}, \quad (2.22)$$

with E_I being the ionization energy of the atom. For $\gamma > 1$ the electron's binding energy is larger than the maximal kinetic energy gained in the laser field. This is the regime of multi-photon ionization, where the rate of n -photon absorption is proportional to I_0^n . In contrast, for $\gamma < 1$ the laser field bends the potential barrier of the atom or molecule so far, that the electron may tunnel through the barrier or even until the electron is quasi free, as illustrated in Fig. 2.2. This is the strong field regime, in which the maximum energy gained in the laser field is larger than the electron's binding energy. It should be noted, that there is no strict transition between the regimes and experiments around $\gamma \approx 1$ exhibit typical features of both mechanisms [10, 52].

According to the Keldysh parameters, listed in Table 2.1, the XUV experiments are clearly situated in the multi-photon regime, while the experiments carried out with the IR laser are better described and understood in the tunneling regime.

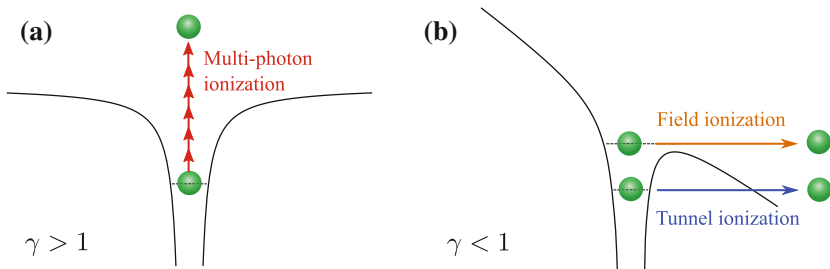


Fig. 2.2 Mechanisms of **a** multi-photon ionization ($\gamma > 1$) and **b** tunnel and field ionization ($\gamma < 1$)

2.2 Many-Electron Systems

In order to describe an atom consisting of N electrons and a nucleus of charge Z , the kinetic energy of all particles and the interaction between them must be taken into account. In a non-relativistic fashion this is done by including all attractive terms from the nucleus-electron interaction and all Coulomb-repulsion terms from the electron-electron interaction into the Hamiltonian²

$$\hat{H} = \sum_{j=1}^N \left(-\frac{1}{2} \Delta_j - \frac{Z}{r_j} + \frac{1}{2} \sum_{k \neq j}^N \frac{1}{r_{jk}} \right) \quad (2.23)$$

with the Laplace operator $\Delta_j = \nabla_j^2$, the distance $r_{jk} = |\mathbf{r}_j - \mathbf{r}_k|$ between the electrons j and k , and the distance $r_j = |\mathbf{r}_j - \mathbf{r}_n|$ between the electrons and the nucleus. The central task is to solve the Schrödinger equation

$$\hat{H} \Psi(q_1, q_2, \dots) = E \Psi(q_1, q_2, \dots), \quad (2.24)$$

in order to get the multi-electron wave function $\Psi(q_1, q_2, \dots)$ with the coordinates $q_i = (\mathbf{r}_i, s_i)$, where \mathbf{r}_i denotes the spatial and s_i the spin coordinates. In the following we will only consider the spatial coordinate. In the mean-field approximation [56] the potential V_j seen by the electron j is approximated by an averaged central potential of all other electrons and the nucleus

$$V_j(r_j) = -\frac{Z}{r_j} + \left\langle \sum_{k \neq j}^N \frac{1}{r_{jk}} \right\rangle. \quad (2.25)$$

Therefore each electron moves in a field of the point-like nucleus and the mean field created by the other $N - 1$ electrons. The motion of a single electron is independent of the motion of the other electrons. This allows a separation ansatz for the multi-electron wave function consisting of single-electron wave functions $\phi_i(\mathbf{r}_i)$:

$$\psi(\mathbf{r}_1, \mathbf{r}_2, \dots) = \phi_1(\mathbf{r}_1) \phi_2(\mathbf{r}_2) \dots \phi_N(\mathbf{r}_N). \quad (2.26)$$

The single-electron wave functions, also called orbitals, are obtained by solving the single-particle Schrödinger equations with the averaged potentials $V_j(r_j)$. These potentials can only be determined precisely by integrating over the density of all other orbitals, which are generally not known. Therefore, the Schrödinger equation may be iteratively solved via the variational Hartree-method [35]. One starts with a set of single-particle wave functions, which are expanded in an appropriate basis set and assumes some initial averaged potential for each electron. In every iteration

² If not indicated otherwise, the presentation given here follows that of [38].

step the Schrödinger equation is solved and the computed orbitals are compared to those of the previous step. If the agreement is not good enough, a modified potential is calculated and the next iteration is started by calculating new orbitals. Only if self-consistency [61] is reached, meaning the previous and present orbitals agree (up to a predefined accuracy), the iteration stops. In the end, one obtains a set of N orbitals $|\phi_i(r_i)\rangle$, called an electron configuration, which allows the determination of the total energy of the electron configuration

$$E = \langle \phi_1(\mathbf{r}_1)\phi_2(\mathbf{r}_2) \dots \phi_N(\mathbf{r}_N) | \hat{H} | \phi_1(\mathbf{r}_1)\phi_2(\mathbf{r}_2) \dots \phi_N(\mathbf{r}_N) \rangle. \quad (2.27)$$

2.2.1 Hartree–Fock Method

So far, the fact that electrons are indistinguishable particles and fermions, and consequently that their total wave function has to be antisymmetric, has not been taken into account. This is taken care of in the Hartree–Fock formalism by using the Slater determinant

$$\Psi(q_1, q_2, \dots, q_N) = \frac{1}{\sqrt{N!}} \begin{vmatrix} \phi_\alpha(q_1) & \phi_\beta(q_1) & \dots & \phi_\nu(q_1) \\ \phi_\alpha(q_2) & \phi_\beta(q_2) & \dots & \phi_\nu(q_2) \\ \vdots & \vdots & \ddots & \vdots \\ \phi_\alpha(q_N) & \phi_\beta(q_N) & \dots & \phi_\nu(q_N) \end{vmatrix}, \quad (2.28)$$

which guarantees the required symmetry properties. The $\phi_\lambda(q_i)$ are single electron wave functions, where λ denotes a set of quantum number $(n_l m_l m_s)$ and $q_i = (\mathbf{r}_i, s_i)$. In the following we will only consider the spatial coordinates.

The Hartree–Fock Hamiltonian \hat{F} is expressed in terms of single-electron Hamiltonians \hat{f}_i consisting of $\hat{h}_i = -\frac{1}{2}\Delta_i - \frac{Z}{r_i}$ and the electron-electron interaction $\hat{v}_i = \hat{j}_i - \hat{k}_i$:

$$\hat{F} = \sum_i \hat{f}_i \quad \text{with} \quad \hat{f}_i = \hat{h}_i + \hat{v}_i, \quad (2.29)$$

with the Coulomb operators \hat{j}_i and the exchange operators \hat{k}_i defined via their action on a single electron wave function ϕ_λ [86]:

$$\hat{j}_i(r_n)\phi_\lambda(r_n) = \left[\int \phi_i^\dagger(r_m) \frac{1}{|r_{nm}|} \phi_i(r_m) d^3r_m \right] \phi_\lambda(r_n), \quad (2.30)$$

$$\hat{k}_i(r_n)\phi_\lambda(r_n) = \left[\int \phi_i^\dagger(r_m) \frac{1}{|r_{nm}|} \phi_\lambda(r_m) d^3r_m \right] \phi_i(r_n). \quad (2.31)$$

The N -electron wave function is found by solving the Hartree–Fock equation

$$\hat{F}|\Psi\rangle = E_{\text{HF}}|\Psi\rangle. \quad (2.32)$$

When deriving the total energy $E_{\text{HF}} = \langle \Psi(q_1, q_2, \dots, q_N) | \hat{F} | \Psi(q_1, q_2, \dots, q_N) \rangle$ of a certain electron configuration, using the Slater determinant from Eq. (2.28) and the Hamiltonian from Eq. (2.29), one arrives at

$$E_{\text{HF}} = \sum_{\nu} \epsilon_{\nu}, \quad (2.33)$$

with the energy of an individual orbital ν being

$$\epsilon_{\nu} = E_{\nu\nu} + \sum_{\lambda \neq \nu} V_{\nu\lambda[\nu\lambda]}. \quad (2.34)$$

Here, $E_{\nu\nu} = \langle \phi_{\nu} | \hat{h}_{\nu} | \phi_{\nu} \rangle$ is the single-electron energy in the field of the nucleus and $V_{\nu\lambda[\nu\lambda]} := V_{\nu\lambda\nu\lambda} - V_{\nu\lambda\lambda\nu}$ is the electron-electron Coulomb matrix element consisting of two terms [86]:

$$\text{Direct term:} \quad V_{\nu\lambda\nu\lambda} = \iint \phi_{\nu}^{\dagger}(r_i) \phi_{\lambda}^{\dagger}(r_k) \frac{1}{|r_{ik}|} \phi_{\nu}(r_i) \phi_{\lambda}(r_k) d^3r_i d^3r_k, \quad (2.35)$$

$$\text{Exchange term:} \quad V_{\nu\lambda\lambda\nu} = \iint \phi_{\nu}^{\dagger}(r_i) \phi_{\lambda}^{\dagger}(r_k) \frac{1}{|r_{ik}|} \phi_{\lambda}(r_i) \phi_{\nu}(r_k) d^3r_i d^3r_k. \quad (2.36)$$

The direct term corresponds to the energy of an electron in the averaged field of another electron. The exchange term arises from the fact that the electrons are indistinguishable and describes their exchange.

The Hartree–Fock equation in Eq. (2.32) consists of a set of N coupled single-particle differential equations $\hat{f}_i \phi_i(r_m) = \epsilon_i \phi_i(r_m)$ that cannot be solved analytically. Thus, in practice, the solution is found via a self-consistent iterative method as introduced in the previous section: A set of basis functions is chosen in which each single-electron wave function ϕ_i is expanded. The variation consists of modifying the expansion coefficients in each iteration step and thereby finding the best suited orbitals (single-particle wave functions). In order to do so a large amount of integrals of the type of Eqs. (2.35) and (2.36) must be calculated. It should be emphasized that the quality of the single-particle wave functions strongly depends on the chosen basis set [19]. However if the complexity of the basis functions increases, which is needed to correctly describe many-electron configurations correctly, the computational effort increases strongly. A compromise between accuracy and calculation time is usually made by choosing a standard basis set, such as Slater functions or Gauß functions. In particular the latter type of basis function allows fast calculations due to the advantageous integration properties of Gauß functions. More details can for instance be found in [46].

2.2.2 Electron Correlation

The Hartree–Fock method allows to account for the nucleus–electron interaction precisely and treats electron–electron interaction by an approximated overall potential seen by each electron. However, this picture of independently behaving electrons is not completely accurate as effects like autoionization (cf. Sect. 2.4), which rely on the correlation between the electrons in the atom, are impossible to describe in the Hartree–Fock picture.

One method to account for electron correlation³ is the so-called Configuration Interaction (CI) method [70] where the multi-electron wave function is a linear combination of Slater determinants (electron configurations). Thus, the total wave function Ω is a superposition of different electron configurations Ψ_k , which can each be obtained by the Hartree–Fock method:

$$\Omega = \sum_k c_k \Psi_k. \quad (2.37)$$

The central task consists of finding the optimal coefficients c_k , which can again be done iteratively, as introduced before.

Usually the expansion contains a leading term, the Hartree–Fock ground-state configuration, and further excited configurations, created by substituting filled orbitals with empty ones. Depending on how many substitutions are performed one speaks about single excitation for one and double excitation for two substitutions. In the literature, e.g., [66], the different configurations are referred to as n -hole and m -particle ($nhmp$) configurations with n being the number of considered excitations with respect to the ground state and m being the number of excited electrons. Thus, a $1h1p$ -state is singly excited compared to the reference ground state. If the ground state is already composed of more than one Slater determinant, one speaks of a multi-reference CI calculation (MRCI) [78]. If all excited states are taken into account, a full-CI calculation is performed, however this is only feasible for very small systems [6].

Another method, that can be used to construct the wave function in a basis of correlated electron states is the so-called Algebraic Diagrammatic Construction (ADC) method [69]. It is based on the Green’s function formalism that is applicable to describe transitions in many-electron systems including correlation effects [17]. In order to describe a transition from an initial to a final state the wave functions of the participating states were so-far derived separately. The Green’s function method allows to calculate energy differences and transition amplitudes directly. However, the Green’s function cannot be calculated exactly due to the high complexity of many electron systems, thus one chooses a perturbative approach in which the total Hamiltonian is split into a non-perturbed and an interaction part. One way to determine the Green’s function in the framework of perturbation theory is the ADC method. Thus,

³ The presentation in this chapter follows [19, 86].

if all orders of the expansion were taken into account the resulting wave functions would be exact. The expansion is truncated at a given order n , which is then denoted as an ADC(n) scheme. The ADC(2) scheme, for instance, describes singly ionized systems (one hole) with a wave function including all 1h0p and 2h1p contributions.

2.2.3 Diatomic Molecules

Diatomic molecules, consisting of two atoms, A and B, are described by considering the kinetic energies of all constituents and the interaction between them.⁴ The kinetic energies of the nuclei and the electrons is given by

$$\hat{T}_N = -\frac{1}{2\mu} \Delta_R \quad \text{and} \quad \hat{T}_e = -\frac{1}{2} \sum_i^N \Delta_{r_i}, \quad (2.38)$$

with the reduced nuclear mass $\mu = M_A M_B / (M_A + M_B)$, the internuclear distance vector $\mathbf{R} = \mathbf{R}_B - \mathbf{R}_A$, and \mathbf{r}_i the electrons' distance vectors from the center of mass. Thus, the Hamilton operator reads

$$\hat{H} = \hat{T}_N(\mathbf{R}) + \hat{T}_e(\mathbf{r}) + V(\mathbf{R}, \mathbf{r}), \quad (2.39)$$

with the potential

$$V(\mathbf{R}, \mathbf{r}) = V_{Ae} + V_{Be} + V_{ee} + V_{AB} \quad (2.40)$$

$$= -\sum_{i=1}^N \frac{Z_A}{|\mathbf{r}_i - \mathbf{R}_A|} - \sum_{i=1}^N \frac{Z_B}{|\mathbf{r}_i - \mathbf{R}_B|} + \sum_{i < k}^N \frac{1}{|\mathbf{r}_i - \mathbf{r}_k|} + \frac{Z_A Z_B}{R}. \quad (2.41)$$

In order to describe the system, the stationary Schrödinger equation $\hat{H}\Psi(\mathbf{r}, \mathbf{R}) = W\Psi(\mathbf{r}, \mathbf{R})$ must be solved, where W is the total energy of the system. No analytical solution exists, even for the smallest molecule H_2^+ , calling for a numerical solution. However, by introducing reasonable approximations, the Schrödinger equation may be significantly simplified. The most important complexity reduction is achieved by applying the so-called Born–Oppenheimer approximation [13]. It allows the separation of the Schrödinger equation into one equation for the electrons and one for the nuclei. Neglecting the coupling between electronic and nuclear motion is possible, because the electronic motion is roughly a factor of 1,000 faster than that of the nuclei. Therefore, electrons adapt virtually immediately to the movement of the nuclei and the electronic wave function is solved for stationary interatomic distances R . The product ansatz $\Psi(\mathbf{r}, \mathbf{R}) = \phi(\mathbf{r})\chi(\mathbf{R})$ leads to the decoupling of the Schrödinger equation into an electronic and a nuclear part:

⁴ The presentation given in this section is compiled from [19, 34, 39].

$$\text{Electronic:} \quad \left(\hat{T}_e + V(\mathbf{r}, \mathbf{R}) \right) \phi(\mathbf{r}) = W_\gamma(\mathbf{R}) \phi(\mathbf{r}), \quad (2.42)$$

$$\text{Nuclear:} \quad \left(\hat{T}_N + W_\gamma(\mathbf{R}) \right) \chi(\mathbf{R}) = W_{\gamma,\nu} \chi(\mathbf{R}). \quad (2.43)$$

$W_\gamma(R)$, depending on a set of electronic quantum numbers γ , denotes the R -dependent eigenvalues of the electronic Schrödinger equation, which serve as the potential of the nuclear Schrödinger equation. The R -dependent behavior of $W_\gamma(R)$ is known as a molecular potential energy curve, which will be denoted as $V(R)$ for the rest of this work. All potential energy curves show a steep rise for small R due to the repulsion of the nuclei and converge to the asymptotic behavior of separated atoms or ions for large R . Bound molecular states exhibit a potential minimum at an intermediate R , which is the equilibrium internuclear distance R_{eq} . The eigenvalues of the nuclear equation $W_{\gamma,\nu}$ correspond to the total energy of a molecular state with a set of electronic quantum numbers γ and a set of nuclear quantum numbers ν . The total energy of a molecule is composed of three different contributions:

$$W_{\gamma,\nu} = W_\gamma(\mathbf{R}) + W_{\text{vibration}}(\mathbf{R}) + W_{\text{rotation}}(\mathbf{R}) = \text{const.} \quad (2.44)$$

Each term has its characteristic energy and time scale. The binding energies of electronic states are usually in the order of several electronvolt and the motion of electrons takes place within tens to hundreds of attoseconds. Vibrational states exhibit typical energies in the order of 0.1 eV and the time scales range from a few to hundred femtoseconds. The binding energies of rotational states are even lower and rotation periods are in the order of picoseconds.

Within this work typical time scales of vibrational motion will be investigated, while rotations will not be considered. If the vibration of a molecule is a small displacement around R_{eq} , a Taylor expansion around that distance leads to

$$V_\gamma(R) = V_\gamma(R_{\text{eq}}) + (R - R_{\text{eq}}) \left. \frac{dV_\gamma}{dR} \right|_{R=R_{\text{eq}}} + \frac{1}{2} (R - R_{\text{eq}})^2 \left. \frac{d^2V_\gamma}{dR^2} \right|_{R=R_{\text{eq}}} + \dots \quad (2.45)$$

As $\left. \frac{dV_\gamma}{dR} \right|_{R=R_{\text{eq}}}$ vanishes at the potential minimum, we arrive at the potential of an harmonic oscillator

$$V_\gamma(R) = V_\gamma(R_{\text{eq}}) + \frac{1}{2} k (R - R_{\text{eq}})^2, \quad (2.46)$$

with the coupling constant $k = \left. \frac{d^2V_\gamma}{dR^2} \right|_{R=R_{\text{eq}}}$.

Classically, this potential leads to vibrations with the frequency $\omega = \sqrt{\frac{k}{\mu}}$. The solution of the corresponding Schrödinger equation yields the Hermitian polynomials [19]. A harmonic potential is the most basic assumption for a molecular potential. A better estimate is usually gained with the Morse potential [53], while weakly bound systems, such as Ne_2 , are well characterized by a Lennard-Jones potential [41].

We will now consider transitions between vibrational levels of different electronic states m and k . The vibrational and rotational quantum numbers will be denoted as ν and J respectively. The transition matrix element with the nuclear wave functions χ_i is given by

$$\mathbf{D}_{mk} = \int \chi_m^* \mathbf{D}_{mk}^{el} \chi_k d^3 R', \quad (2.47)$$

with \mathbf{D}_{mk}^{el} being the electronic matrix element, which depends on the electronic dipole moment. The nuclear wave function separates into a vibrational part $S_{\text{vib}}(R)$, which is only dependent on R , and a rotational part $Y_J^M(\theta, \phi)$, which depends on the polar angle θ and the azimuthal angle ϕ . Thus, \mathbf{D}_{mk} reads

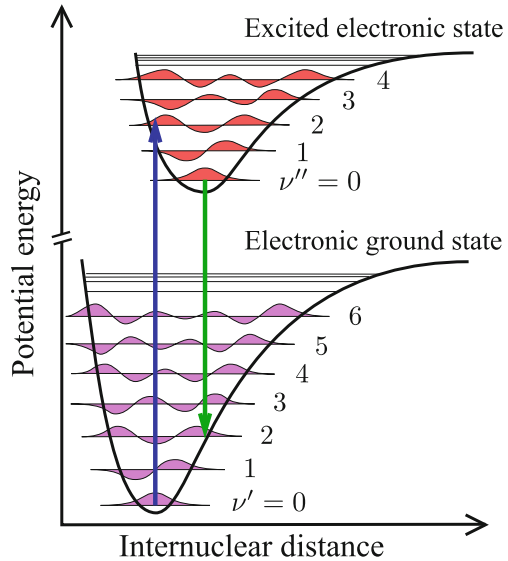
$$\mathbf{D}_{mk} = \int S_{\text{vib}}(\nu'') \mathbf{D}_{mk}^{el} S_{\text{vib}}(\nu') R^2 dR \iint Y_{J''}^{M''} Y_{J'}^{M'} d \cos \theta d\phi. \quad (2.48)$$

If the dipole operator is independent of R , it is moved out of the integral and the absolute square of the first integral can be written as:

$$q_{\nu', \nu''} = \left| \int S_{\text{vib}}(\nu'') S_{\text{vib}}(\nu') R^2 dR \right|^2, \quad (2.49)$$

which is known as the Franck–Condon factor. Thus, the probability for a transition from one vibrational level to another is determined by the spatial overlap of the vibrational wave functions, as illustrated in Fig. 2.3. The second integral in Eq. (2.48)

Fig. 2.3 Illustration of the Franck–Condon principle. The *blue* arrow (pointing upwards) indicates a (*vertical*) Franck–Condon transition from the vibrational and electronic ground state of the molecule into an excited electronic state. Mostly the second excited vibrational state ($\nu'' = 2$) is populated due to the large overlap with the nuclear wave function of the ground state. The *green* arrow (pointing downwards) shows a relaxation of the molecule. Figure adapted from [81]



is the so-called Hönl–London factor, which depends on the rotational quantum numbers. The transition between two vibrational levels via the absorption of a photon is occurring so fast, that the internuclear distance and kinetic energies of the nuclei are considered as fixed. Therefore, these transitions occur on vertical lines at a fixed distance R , which is known as the Franck–Condon principle (cf. Fig. 2.3). Nuclear dynamics within a molecule is often described by a nuclear wave packet propagating in time. The coherent superposition of several vibrational states, that may be populated by photoionization, leads to the modulation of the nuclear wave packet propagating along the internuclear distance.

Solving the multi-electron Schrödinger equation of molecules relies on the methods presented in Sects. 2.2.1 and 2.2.2 for multi-electron atoms. The ansatz for the total wave function is again the product of single-electron wave functions. However, the single electron wave functions are so-called molecular orbitals, which are expressed as linear combinations of atomic orbitals.

The molecular orbitals have more complex symmetry properties when the system is not central symmetric anymore. Due to the symmetry breaking, the characterization of electronic states is more complicated. Here, we will only introduce the nomenclature of electronic states in diatomic homonuclear molecules, as those are relevant for our experimental investigation:

$$^{2S+1}\Lambda_{(g,u)}^{(+,-)}, \quad (2.50)$$

where Λ is the angular momentum and S is the total spin, resulting in the multiplicity $2S + 1$ of each state. The angular momentum is commonly denoted similarly to atoms with Σ, Π, Δ for $\Lambda = 0, 1, 2$. The superscript $(+, -)$ and the subscripts (g, u) indicate symmetry properties of the wave function Ψ . For diatomic molecules, reflection on a plane through the axis of the nuclei, denoted by the operator σ , is a symmetry operation. As applying this reflection operator twice leads to the original wave function,

$$\sigma(\sigma\Psi) = \sigma^2\Psi = \Psi, \quad (2.51)$$

one finds that $(+, -)$ are the eigenvalue of σ :

$$\sigma\Psi = \pm\Psi. \quad (2.52)$$

For diatomic homonuclear molecules another symmetry operation can be defined, inversion I on the center of mass:

$$I^2\Psi = \Psi \quad \text{with} \quad I\Psi_g = +\Psi_g \quad \text{and} \quad I\Psi_u = -\Psi_g. \quad (2.53)$$

Thus, g -states have “gerade” and u -states have “ungerade” symmetry. As an example, the ground state X in H_2 is denoted by $X^1\Sigma_g^+$.

Atoms with closed atomic shells, i.e., the rare gases, are not able to form covalent bonds due to the lack of unpaired valence electrons. Nevertheless, they are able to

assemble in weakly bound structures because of the attractive van-der-Waals forces. Neutral atoms do neither have a net charge nor a dipole moment, when averaged over time. The situation changes if an atom A approaches atom B and the momentary induced dipole moment creates an electric field at B and vice versa. This results in an attractive potential energy of [19]

$$E_{\text{pot}} \propto \frac{\alpha_A \alpha_B}{R^6}, \quad (2.54)$$

where α_A and α_B are the polarisabilities of the respective atoms. Van-der-Waals bonds are weaker than hydrogen bonds and roughly a factor of 100–1,000 weaker than typical chemical bonds. This results in very shallow potential energy curves with only few vibrational states. Therefore, rare gas dimers are usually only stable at low temperatures. The most remarkable example is the He dimer, which has a mean internuclear distance of 52 Å and a binding energy of 95 neV $\hat{=}$ 1.1 mK [32].

2.3 Photoionization for High Photon Energies

In photoionization, the energy of a photon, $\hbar\omega$, is transferred to a bound electron that is consequently ejected into the continuum. For an atom A with the initial state $|a\rangle = |nl\rangle$ and the continuum state $|b\rangle = |\epsilon l'\rangle$, the reaction reads

$$A + \hbar\omega \rightarrow A^+ + e^-. \quad (2.55)$$

The kinetic energy ϵ of the ejected electron equals the photon energy minus the binding energy of the electron: $\epsilon = \hbar\omega - W_I$. The probability for the absorption of a photon is proportional to the transition matrix amplitude $\hat{T}_{ab} = \langle b | \hat{T} | a \rangle$, which is derived via first-order perturbation theory, as presented in Sect. 2.1. The cross section for the process is given by

$$\sigma_{ab}(\hbar\omega) = 4\pi^2 \alpha \hbar\omega \left| \hat{T}_{ab} \right|^2. \quad (2.56)$$

For large photon energies, where $W_I \ll \hbar\omega \ll mc^2$, and for one-electron systems, the wave function of the outgoing electron can be approximated by a plane wave. Further assuming hydrogen-like radial wave functions, the total cross section for photoionization reads [38]:

$$\sigma_{ab} \propto \frac{Z^5}{n^3 (2\hbar\omega)^{7/2}}. \quad (2.57)$$

This formula illustrates some of the characteristic features in photoionization cross sections, such as the strong decrease with the photon energy and the increase for heavier nuclei. In addition the removal of electrons from outer orbitals is preferred.

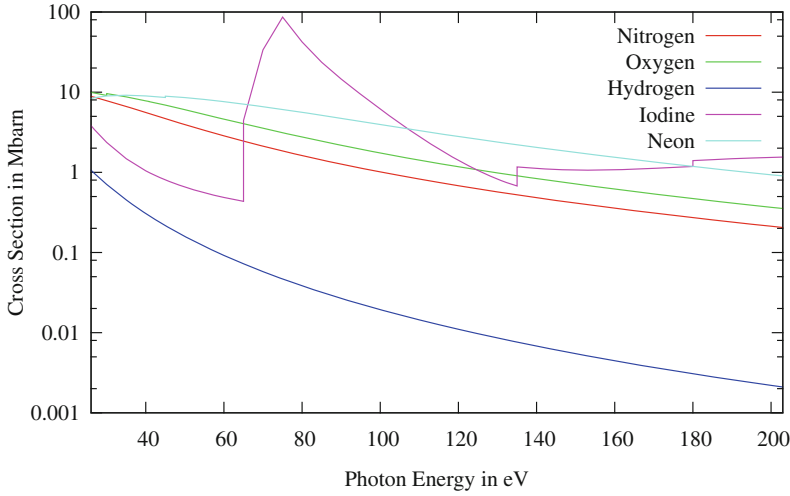


Fig. 2.4 Photoionization cross sections of background species nitrogen, oxygen and hydrogen, and the target species iodine and neon [83]

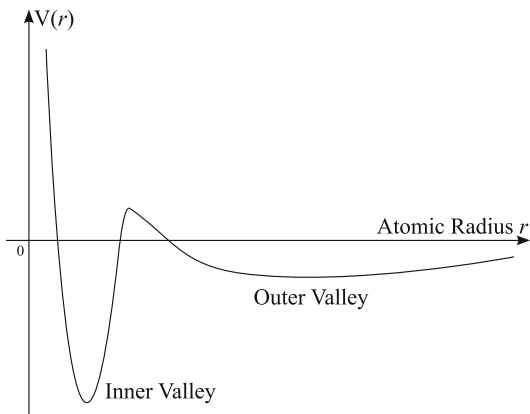
Figure 2.4 shows the cross sections for relevant background species and the investigated targets as a function of the photon energy. The aforementioned features are clearly present in these spectra. However, iodine shows an exceptional behavior with a distinct maximum above 80 eV and further steps at photon energies of 140 and 180 eV. These characteristic steps can usually be attributed to the break-up of an additional shell, e.g., the photon energy overcomes the ionization potential of the electrons sitting in the next tighter bound shell. At these so-called absorption edges the cross section is usually maximal and drops off afterwards. In iodine the step at 140 eV corresponds to the break-up of the $4p$ shell, while the 180 eV step corresponds to that of the $4s$ shell. The broad maximum in the cross section above 80 eV is assigned to a so-called shape resonance, which will be discussed in the following.

2.3.1 $4d$ Shape Resonance

The observed increase in the photoionization cross section of I in a broad region above 80 eV is assigned to the excitation of a $4d$ shape resonance [73]. Here, we will give an intuitive explanation for this effect [15, 18]. The effective potential of atoms other than hydrogen is given by a Coulomb potential modified by a repulsive centrifugal term:

$$V_{\text{eff}}(r) = -\frac{Z}{r} + \frac{l(l+1)}{2r^2}, \quad (2.58)$$

Fig. 2.5 Double valley potential, that may lead to the formation of a shape resonance: The $4f$ wave function collapses from the *outer* well into the *inner* well, where the $4d$ wave function is localized



with l being the angular momentum quantum number of the respective electronic state. For certain combinations of Z and l , particularly for the $4f$ shell in iodine, a potential with the eponymous *shape*, a so-called *double valley* (cf. Fig. 2.5), may arise. In this situation the $4f$ wave function may *collapse* from the outer well (where all nf states would be expected) into the inner well, leading to an increased spatial overlap with the $4d$ wave function, which is localized in the inner well. Due to the enhanced overlap, exciting a $4d$ electron by photoabsorption will most likely induce a transition to $4f$, while a transition to the spatially separated nf for $n > 4$ is very unlikely. The resulting $4f$ state lies above the ionization potential and will thus autoionize, as discussed in Sect. 2.4. In conclusion, we note that if the initial and the final state overlap perfectly, due to the collapse of the latter, a strong increase in the cross section for this transition occurs, a so-called *giant* resonance. In fact, this is the case for the $4d$ and the $4f$ wave functions in Xe and I.

2.4 Relaxation Processes in Atoms and Molecules

The removal of electrons from outer-valence shells usually leaves the created ions in their ground state and therefore does not trigger further relaxation dynamics in atoms and molecules. If instead excited ions are produced, due to vacancies in an inner-valence or core shell or due to excited outer-valence electrons, the system may relax via different pathways.

Figure 2.6 shows different relaxation mechanisms for ionized and simultaneously excited atoms. The presented processes can equally well take place in molecules and are not limited to atoms. Due to electron correlation, one photon may also excite two electrons into the continuum at the same time, as shown in Fig. 2.6a. If one of the electrons relaxes, it transfers its energy to the other excited electron, which is consequently ejected. This process is called autoionization and has typical decay

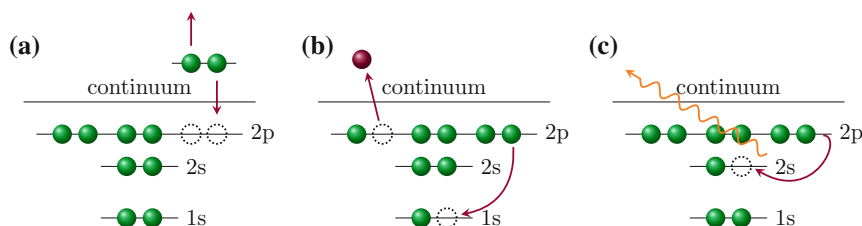


Fig. 2.6 Illustration of the relaxation mechanisms that may occur in excited atoms and molecules. **a** Autoionization **b** Auger decay **c** Radiative decay

times of a few femtoseconds. As autoionization is usually indistinguishable from direct photoionization of the valence shell, these two pathways may interfere and give rise to the famous Fano-resonance line shapes [25].

Depending on the atomic number Z and the binding energy of the electrons, inner-valence and core vacancies relax via two different mechanisms. For intermediate Z (or inner-valence vacancies in high- Z atoms), the dominating effect is Auger decay [51], as illustrated in Fig. 2.6b: An outer-valence electron fills the core hole and the energy released upon the relaxation is transferred to another valence electron, which is then ejected. In larger atoms the entire relaxation process may involve several electrons, resulting in Auger cascades. The ion is still excited after the first Auger decay and relaxes via further Auger decays. For instance the $4d$ vacancy in I_2^+ mostly relaxes via a single or a cascade of two Auger decays [12]. The typical time scales of Auger decay are a few femtoseconds. Note that autoionization and Auger decay are possible due to the Coulomb interaction between the electrons involved in the processes.

For core holes in heavy elements, radiative decay, as shown in Fig. 2.6c, is usually the dominating relaxation pathway, with typical lifetimes in the order of a few femtoseconds [4]. For light elements, Auger decay is often energetically forbidden and the only remaining relaxation pathway is radiative decay. There, excited states often have lifetimes in the pico- to nanosecond regime. Notably, the lifetime of a $\text{Ne}^+(2s^{-1})$ ion is 0.2 ns [31].

2.5 Interatomic Coulombic Decay

The lifetimes of core vacancies in strongly bound molecules and solids can be affected by the environment, which is known as chemical shift [48]. However the effect is weak and van-der-Waals and hydrogen bonds have hardly any influence on the dynamics of core- and inner-valence vacancies. Despite these findings, a new relaxation mechanism for inner-valence ionized atoms and molecules embedded into a weakly interacting environment was proposed in 1997: interatomic or intermolecular Coulombic decay (ICD) [16]. The vacancy is filled by an outer-valence electron and the released energy is transferred to a neighboring particle, which then emits an electron.

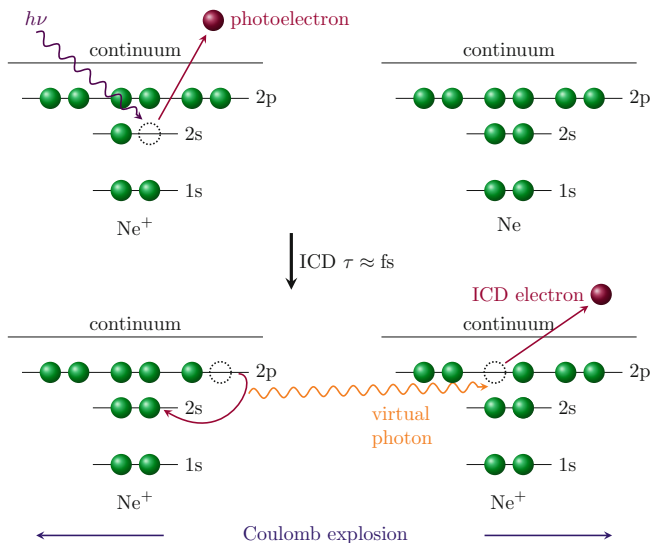


Fig. 2.7 Illustration of the ICD process in Ne_2 dimers. A $2s$ electron in either of the two Ne atoms is removed. The relaxation energy of 27.2 eV (insufficient for the removal of a $2p$ electron in the same ion) is transferred to the neutral Ne atom via virtual photon exchange. Since a $2p$ electron in the neutral Ne is bound with only 21.6 eV, the excess energy is large enough to ionize the formerly neutral side of the dimer. The final state consists of two singly charged Ne^+ ions, which Coulomb explode

In 2003, ICD was first experimentally confirmed in large neon clusters [49] via a low-energetic feature in the electron spectra, which was not present for monomers. A further proof of ICD was given in 2004 by a kinematically complete experiment on Ne_2 [40]. The process is depicted in Fig. 2.7: An isolated $2s$ inner-valence ionized Ne^+ ion can only relax radiatively, which occurs within 0.2 ns, because Auger decay is energetically forbidden. If another Ne atom is placed nearby, the hole is filled by a $2p$ electron and the excess energy is transferred to the neighboring atom, which is consequently ionized. The relaxation energy of 27 eV is not sufficient to remove a second electron from the ion, which requires more than 40 eV. However it is sufficient to remove a $2p$ electron from a neutral Ne atom, which is bound with 21 eV. Finally, two singly charged Ne^+ ions are produced, which repel each other with the Coulomb force. The process is possible because the double ionization threshold in clusters is considerably lowered compared to monomers as the charges can be distributed among the constituents.

By now, a whole plethora of ICD phenomena in different systems was predicted and many of them have been experimentally verified. In the following, we discuss the processes relevant for Ne_2 . An overview of the experimental status of ICD research can be found in [37], a review on ICD theory is given in [3].

2.5.1 Theoretical Treatment

The goal of our experiment on Ne_2 is the determination of the lifetime τ of the excited $\text{Ne}_2^+(2s^{-1})$ state. The probability p for finding the system in the excited state at a certain time t is given by

$$p = p_0 e^{-\frac{\Gamma t}{\hbar}} \quad \text{with } p_0 = p(t=0). \quad (2.59)$$

While the obvious choice of observable from the experiment is the lifetime, theory prefers the decay width $\Gamma = \hbar/\tau$. Besides Γ , electron and ion spectra for comparison with the experiment may be calculated.

The theoretical treatment of ICD is a challenging task as it requires the full quantum mechanical description of a many electron system for which electron correlation must be taken into account. Moreover, nuclear motion occurring while the decay takes place, must be included. In order to gain further insight into the ICD mechanism, we begin in Sect. 2.5.1.1 by giving an expression for Γ derived within the framework of time-dependent perturbation theory via the Wigner–Weißkopf method, following the presentation in [66]. Since this method is not routinely applied for the determination of decay widths, a brief discussion of other methods will be given in Sect. 2.5.1.2. An overview of the existing calculations for the $2s^{-1}$ vacancy in Ne_2^+ , is presented in Sect. 2.5.1.3. In order to obtain a complete theoretical treatment for ICD, nuclear motion must be included, which will be introduced in Sect. 2.5.1.4.

2.5.1.1 Wigner–Weißkopf Method

An expression for the decay width Γ_{iv} of an inner-valence ionized system, such as $\text{Ne}_2^+(2s^{-1})$, may be derived by applying the Wigner–Weißkopf method [66, 77]:

$$\begin{aligned} \Gamma_{\text{iv}} = 2\pi \sum_k \sum_{\text{ov}_1} \sum_{\text{ov}_2 > \text{ov}_1} & \underbrace{|V_{\text{ov}_1, \text{ov}_2[\text{iv}, k]}|^2}_{(a)} \\ & \times \delta(\epsilon_{\text{iv}} - \underbrace{\epsilon_{\text{ov}_1} - \epsilon_{\text{ov}_2} + V_{\text{ov}_1, \text{ov}_2[\text{ov}_1, \text{ov}_2]}}_{(b)} + \underbrace{\epsilon_k - V_{k, \text{ov}_1[k, \text{ov}_1]} - V_{k, \text{ov}_2[k, \text{ov}_2]}}_{(c)}), \end{aligned} \quad (2.60)$$

with the summation indices k for the continuum, iv for the inner-valence hole, ov_1 and ov_2 for the first and the second outer-valence hole, respectively. Energies are denoted by ϵ . The notation $V_{pq[rs]} = V_{pqrs} - V_{pqsr}$ for the direct and the exchange terms respectively has been introduced in Sect. 2.2.

We will first discuss the argument of the delta function, which ensures energy conservation and thus specifies the possible decay channels of the inner-valence vacancy. The binding energy ϵ_{iv} of the ejected inner-valence electron, i.e., the total energy available, is distributed among the terms (b) and (c). Term (b) corresponds

to the energy of a doubly outer-valence-ionized state consisting of the ionization potentials of the outer-valence electrons $\epsilon_{\text{ov}_{1,2}}$ and the Coulomb interaction between the holes. This term illustrates why ICD is possible: The double ionization threshold of clusters is lower than that of monomers. Therefore the decay becomes energetically allowed as the outer-valence holes can be placed at two “distant” monomers, which lowers the Coulomb repulsion of the holes. If both electrons were removed from the same monomer, the required energy would be higher than the available $-\epsilon_{\text{iv}}$ and consequently the argument of the delta function never vanishes. Term (c) corresponds to the energy of an emitted electron ϵ_k corrected by the interaction with the two holes.

We conclude that the two outer-valence holes must be located at different monomers in order to get a non-vanishing Γ_{iv} and proceed by discussing the overlap matrix elements $V_{\text{ov}_1, \text{ov}_2, [\text{iv}, k]}$, appearing in (a) from Eq. (2.60), which consists of two contributions:

Direct term:

$$V_{\text{ov}_1, \text{ov}_2, \text{iv}, k} = \iint \phi_{\text{ov}_1}^\dagger(\mathbf{x}_1) \phi_{\text{iv}}(\mathbf{x}_1) \frac{1}{|\mathbf{x}_1 - \mathbf{x}_2|} \phi_{\text{ov}_2}^\dagger(\mathbf{x}_2) \phi_k(\mathbf{x}_2) d^3x_1 d^3x_2. \quad (2.61)$$

Exchange term:

$$V_{\text{ov}_1, \text{ov}_2, k, \text{iv}} = \iint \phi_{\text{ov}_1}^\dagger(\mathbf{x}_1) \phi_k(\mathbf{x}_1) \frac{1}{|\mathbf{x}_1 - \mathbf{x}_2|} \phi_{\text{ov}_2}^\dagger(\mathbf{x}_2) \phi_{\text{iv}}(\mathbf{x}_2) d^3x_1 d^3x_2. \quad (2.62)$$

Each matrix element describes one of the physical processes illustrated in Fig. 2.8 for the $\text{Ne}^+(2s^{-1})$ dimer ion. The direct term in Eq. (2.61) corresponds to the situation in which the inner-valence vacancy ϕ_{iv} is filled by an outer-valence electron from the same monomer ϕ_{ov_1} and an outer-valence electron ϕ_{ov_2} from the other monomer is ejected into the continuum ϕ_k . The exchange term in Eq. (2.62) describes a process in which an electron from the neighboring atom ϕ_{ov_2} fills the inner-valence vacancy ϕ_{iv} and an outer-valence electron from the inner-valence side ϕ_{ov_1} is ejected into the continuum ϕ_k . However, for rare gas clusters the exchange term is very weak at equilibrium internuclear distance because the overlap of ϕ_{ov_2} and ϕ_{iv} is more or less negligible. Therefore the direct ICD process dominates by far. It should be noted though that exchange ICD might also occur under certain circumstances, as will be shown in Sect. 7.2.7.

Now we will discuss the general distance dependence of ICD. The orbital overlap of two neighboring atoms—even at large distance R as occurring in van-der-Waals clusters—is usually non-negligible. However, for inner-valence orbitals the assumption of vanishing overlap is reasonable and a power series expansion may be performed:

$$\frac{1}{|\mathbf{x}_1 - \mathbf{x}_2|} = \frac{1}{R} - \frac{(\mathbf{r}_1 - \mathbf{r}_2) \cdot \mathbf{u}_R}{R^2} + \frac{3[(\mathbf{r}_1 - \mathbf{r}_2) \cdot \mathbf{u}_R]^2 - (\mathbf{r}_1 - \mathbf{r}_2)^2}{2R^3} + O\left(\frac{1}{R^4}\right), \quad (2.63)$$

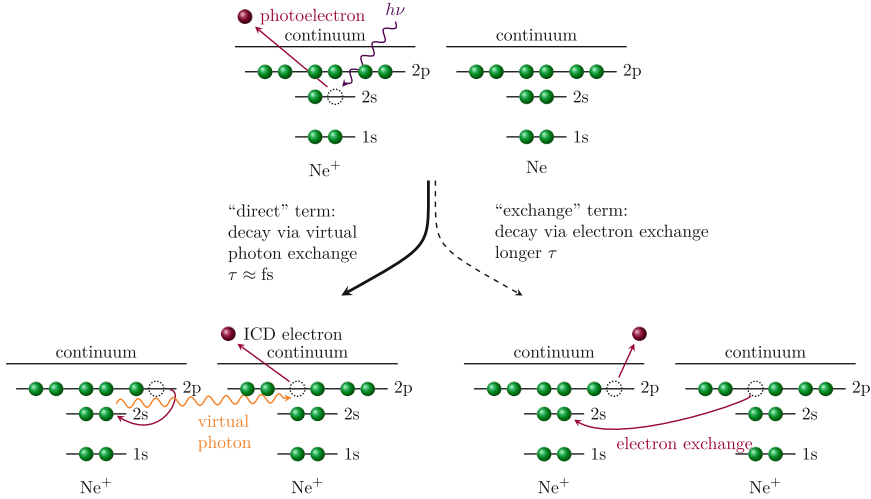


Fig. 2.8 Illustration of the two competing ICD processes: direct ICD and exchange ICD. In the direct process the 2s vacancy at the left neon ion is filled by a 2p electron from the same ion and the excess energy is transferred to a neighboring 2p electron, which is then ejected. In the exchange process the 2s vacancy is filled by a neighboring 2p electron and the released energy is given to a 2p electron at the *left* side, which is then emitted

with $\mathbf{R} = \mathbf{R}_1 - \mathbf{R}_2$, the unit vector \mathbf{u}_R along the internuclear axis and the position \mathbf{r}_i of the electrons relative to the monomers' centers of mass \mathbf{R}_i . If we insert this expansion into Eq. (2.61), the first two terms cancel and the first non-vanishing term is

$$V_{\text{ov}_1, \text{ov}_2, \text{iv}, k} \propto \frac{1}{R^3}. \quad (2.64)$$

Here, one has to assume that $\langle \phi_{\text{ov}_1} | \phi_{\text{iv}} \rangle = \langle \phi_{\text{ov}_2} | \phi_k \rangle = 0$. Therefore, for large R we obtain

$$\Gamma_{\text{iv}} \propto \frac{1}{R^6}. \quad (2.65)$$

The characteristic $1/R^6$ behavior is also known from other intermolecular processes, such as Förster resonances [28] and Penning ionization [58, 72]. In the *Förster Resonant Energy Transfer* (FRET) the excitation energy of one molecule is non-radiatively transferred to a close-by molecule that absorbs the energy and subsequently emits it via fluorescence. The occurrences and applications of FRET are manifold. Notable examples are light harvesting in photosynthesis [27] and the structural and functional studies of proteins [30]. All involved electronic states in FRET are bound, therefore discrete and thus the energy emitted from one molecule must be resonant with the excitation of the other molecule. Achieving the resonance condition often requires nuclear motion, which determines the duration of the process [64]. For (direct) ICD a resonant energy transfer is not required as the electron, which absorbs the relaxation

energy, is ejected into the continuum. Therefore it takes place much faster. Penning ionization is a process occurring in slow ion-atom collisions: An excited atom collides with a neutral one, thereby forming a quasimolecular state for a short time. The excitation energy is transferred to the neutral particle, which is consequently ionized [72].

2.5.1.2 Decay Widths

In practice, ICD widths are usually calculated within two different theoretical frameworks, which are briefly introduced here.⁵ In atomic physics, resonances are, for instance, found in electron scattering with atoms or molecules or in photoionization, resulting in an enhanced cross section for a certain process. Related are autoionization, Auger decay and ICD. Resonances are characterized by their complex Siegert energy [71], consisting of their position on the energy scale E_R and their decay width Γ :

$$E_{\text{res}} = E_R - i\frac{\Gamma}{2}. \quad (2.66)$$

A major difficulty that arises in calculating the lifetime of resonances is the wave function of the outgoing electron. As it is not square integrable, standard electronic structure theory is not applicable [65]. One method is to make the electron wave function square integrable by introducing a Complex Absorbing Potential (CAP), which creates an absorbing boundary condition around the considered molecular system. It is important to note, that the boundary condition must be chosen in such a way that the wave function in the vicinity of the molecule is not disturbed [63]. The absorption of the electron is achieved by adding a complex term to the original Hamiltonian \hat{H} of the system:

$$\hat{H}(\eta) = \hat{H} - i\eta\hat{W}. \quad (2.67)$$

The parameter η is a real positive number and referred to as the CAP strength and \hat{W} is a local semi-definite one-particle operator. The new Hamiltonian still fulfills the Schrödinger equation, but is non-Hermitian. Thus, its eigenvalues are no longer real numbers. Even though the CAP disturbs the Hamiltonian, the exact eigenvalues of the resonance are obtained in the limit of vanishing η [60]. If a complete basis set is given, each resonance has an eigenvalue $E(\eta)$ with

$$\lim_{\eta \rightarrow 0} E(\eta) = E_R - i\frac{\Gamma}{2} \quad (2.68)$$

corresponding to the Siegert energy. Thus, the complex part of the eigenvalue $E(\eta)$ yields the decay width.

⁵ If not indicated otherwise, the presentation given here is compiled from [3, 63, 75].

In order to perform the actual calculation, many-electron wave functions of the initial and final state of the system are needed. The wave functions and, thus, the energy eigenvalues can be determined using different *ab initio* techniques: Two commonly used methods for ICD calculations are the configuration interaction (CI) and the algebraic diagrammatic construction (ADC) [69] method, which have been introduced in Sect. 2.2.2. For a detailed treatment of the CAP-CI method see [66]. The application of CAP-ADC to the $\text{Ne}^+(2s^{-1})$ decay rate is presented in [75].

Another method⁶ used to calculate ICD decay widths is based on the Fano theory of resonances [25]. The wave function Ψ_E at the energy E , which is beyond the ionization energy, is expressed as a superposition of a bound-like state Φ and a continuum-like state χ :

$$\Psi_E = a(E)\Phi + \sum_{\beta=1}^{N_c} \int C_{\beta}(E, \epsilon) \chi_{\beta, \epsilon} d\epsilon. \quad (2.69)$$

The initial state of the decay Φ corresponds to the $\text{Ne}^+(2s^{-1})$ state of our system. $\chi_{\beta, \epsilon}$ is the final state with the continuum energy ϵ and enumerated by β , which counts the decay channels up to N_c . Here, this is the doubly ionized $\text{Ne}^+ - \text{Ne}^+$ state. The decay width Γ is expressed in the Fano theory as:

$$\Gamma = \sum_{\beta=1}^{N_c} \Gamma_{\beta} = 2\pi \sum_{\beta=1}^{N_c} \left| \left\langle \Phi \left| \hat{H} - E_r \right| \chi_{\beta, \epsilon_{\beta}} \right\rangle \right|^2. \quad (2.70)$$

E_r is the energy of the decaying state: $E_r \approx E_{\Phi} = \langle \Phi | \hat{H} | \Phi \rangle$ and ϵ_{β} is the asymptotic kinetic energy of the ICD electron emerging from the decay channel β .

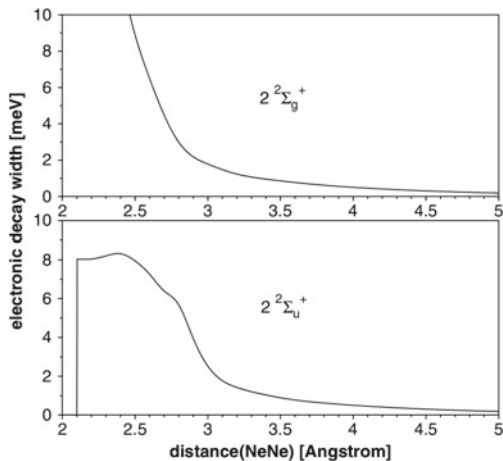
In order to calculate Γ via Eq. (2.70), the wave functions of the initial and the final states are needed. These correlated many-electron states can for instance be constructed via the ADC method [69].

2.5.1.3 Decay Widths for the Neon Dimer

The ICD lifetime of the $2s^{-1}$ vacancy in Ne_2^+ was subject to many theoretical studies, which will be reviewed here. In a study on the dependence of the lifetime on the cluster size, it was shown that the lifetime of the $2s$ hole decreases from $\tau = 85$ fs for Ne_2 down to $\tau = 3$ fs for Ne_{13} [64]. The decay width for the $^2\Sigma_u$ state was calculated using the Stieltjes–Chebyshev moment theory [66]. As the initial and final states were determined via Hartree–Fock calculations, no correlation effects were included and the geometry of the clusters was kept at a fixed solid-neon-like internuclear distance of 3.13 \AA [64].

⁶ This discussion is adapted from [3].

Fig. 2.9 Decay width Γ as a function of the internuclear distance for both intermediate states $^2\Sigma_u$ and $^2\Sigma_g$ calculated via CAP-CI. Figure taken from [65]



Another study [65] found a strong dependence of the decay width on the internuclear distance R in $\text{Ne}^+(2s^{-1})$ for both intermediate inner-valence states $^2\Sigma_u$ and $^2\Sigma_g$, as shown in Fig. 2.9. There, a lifetime of approximately $\tau = 530$ fs at $R = 3.2$ Å for both states was calculated. The result shown in Fig. 2.9 was obtained using the CAP-CI method with a CI expansion for the $\text{Ne}_2^+(2s^{-1})$ state including all one-hole states and their single and double excitations [66]. A more precise CAP calculation with a multi-reference CI (MRCI) expansion yielded a value of $\tau = 64$ fs for the $^2\Sigma_g$ state at $R = 3.2$ Å [63]. However the latter calculation was only performed at a single internuclear distance due to the high computational complexity.

A further study was carried out in the CAP framework to calculate Γ as a function of the cluster size with optimized cluster geometry, and to investigate its dependence on the used basis set for the calculation [75]. With the most accurate basis, the application of the CAP-ADC method yielded a value of $\tau = 92$ fs at $R = 3.2$ Å for the $^2\Sigma_g$ state while the basis set used in [63, 65] gives a slightly smaller lifetime of $\tau = 74$ fs.

Using the Fano-ADC method to determine the ICD decay widths of the $^2\Sigma_g$ state yields a lifetime of $\tau = 82$ fs at $R = 3.2$ Å [2]. These calculations were performed at several internuclear distances, as shown in Fig. 7.19.

Concluding we note that the most accurate results for the τ of $^2\Sigma_g$ at $R = 3.2$ Å are to be expected from the CAP-MRCI (64 fs) [63], the CAP-ADC (92 fs) [75] and the Fano-ADC (82 fs) method [2].

2.5.1.4 Nuclear Dynamics

The previously presented calculations, performed for a fixed internuclear distance, predicted ICD lifetimes in the order of 100 fs, which gives the nuclei enough time to move prior to the decay. Therefore, it is crucial to include nuclear dynamics into

calculations as the decay width is strongly dependent on the internuclear distance (cf. Figs. 2.9 and 7.19). Only if nuclear motion is included, the calculated electron and ion spectra are comparable to experimental data [65, 67]. Since the behavior of $\Gamma(R)$ is non-linear, a non-trivial impact on the lifetime is expected [68].

The theoretical description of ICD is usually performed in the Born–Oppenheimer approximation where the electronic and the nuclear dynamics are decoupled. Thus, the nuclear motion is added on top of the calculated potential energy curves by describing the whole ICD process as transitions of wave packets between different electronic states. In the following, we give an overview of the method of time-dependent propagation of nuclear wave packets, following the description in [3, 67].

The ground state wave packet is instantaneously projected onto the intermediate inner-valence potential energy curve, where it starts to propagate. As the equilibrium internuclear distances of the intermediate inner-valence states are usually located at smaller R , due to the tighter bound of the singly ionized system, the wave packet usually starts to propagate towards smaller R . Simultaneously the decay process sets in and the final state is populated at the same rate as the density drops in the intermediate state. The final wave packets, associated to the different energies of the ICD electron, are generated and start propagating along the repulsive curve of the final state. The wave packet dynamics is described by a set of coupled differential equations (time-dependent Schrödinger equations) with i denoting the initial, d the intermediate and f the final electronic state with the corresponding nuclear wave functions Ψ_i , Ψ_d and Ψ_{mf} , where m counts the different final electronic states:

$$\begin{aligned} i \frac{\partial}{\partial t} |\Psi_i(R, t)\rangle &= \hat{H}_i(R) |\Psi_i(R, t)\rangle, \\ i \frac{\partial}{\partial t} |\Psi_d(R, t)\rangle &= \hat{F}_i(R) |\Psi_i(R, t)\rangle + \hat{H}_d(R) |\Psi_d(R, t)\rangle, \\ i \frac{\partial}{\partial t} |\Psi_{m,f}(R, t, \epsilon)\rangle &= \hat{W}_m(R, \epsilon) |\Psi_d(R, t)\rangle + \left(\hat{H}_{m,f}(R) + \epsilon \right) |\Psi_{m,f}(R, t, \epsilon)\rangle \end{aligned} \quad (2.71)$$

The initial Hamiltonian $\hat{H}_i = \hat{T}_N + \hat{V}_i$ consists of the nuclear kinetic energy \hat{T}_N and the potential energy \hat{V}_i according to the populated potential energy curve. In order to describe the dynamics of the intermediate state, the decay process must be taken into account by introducing a complex part with the decay width Γ : $\hat{H}_d(R) = \hat{T}_N(R) + \hat{V}_d(R) - i\Gamma(R)/2$. The coupling between the initial and final state is taken care of by \hat{F} , which is only a delta function $\delta(t = 0)$ for instantaneous ionization. The coupling strength W_m between the intermediate and the final state is related to the partial decay widths Γ_m via $\Gamma_m(R) = 2\pi \left| \hat{W}_m(R) \right|$ with $\Gamma = \sum_m \Gamma_m$. The final state Hamiltonian reads $\hat{H}_{m,f} = \hat{T}_N(R) + \hat{V}_{m,f}(R)$ and ϵ is the energy of the outgoing electron. In the system of coupled Schrödinger equations, Eq. (2.71), the norm of the intermediate wave packet decreases with increasing time at a rate given by $\Gamma(R)$. This is caused by the non-hermiticity of \hat{H}_d . The norm of the final wave packet increases accordingly with the same rate. Thus, the norm of the total wave function

for the whole system is constant in time. When the entire wave packet has decayed from the intermediate to the final state, all the information required to compute the ICD electron spectrum and the kinetic energy release for the fragments formed after Coulomb explosion is contained in the final wave packet [67, 68]. Results from calculations including nuclear dynamics, are discussed in Sect. 7.2.8.

2.6 Classical Treatment of the Pump-Probe Technique

No detector is able to resolve processes in the femtosecond time domain, in particular the motion of nuclei in molecules. Therefore dedicated experimental techniques have to be developed, such as the pump-probe method for which Ahmed Zewail was awarded the Nobel Prize in chemistry in 1999 [84]. A preceding pump pulse initiates a certain reaction by populating intermediate states and a probe pulse samples the evolution of the system by further ionizing it at an adjustable time delay. As the achievable temporal resolution lies in the order of the pulse duration, femtosecond pulses are needed to observe nuclear motion in real time. Typical Ti:Sa lasers, operating at 800 nm, deliver pulse durations of 25 fs, which can be further shortened to ≈ 6 fs by spectral broadening [26]. Therefore, even fast molecular processes are accessible via pump-probe spectroscopy in the IR regime [24].

Only in recent years the creation of ultra-short pulses in the XUV to X-ray regime became feasible due to the development of HHG sources [47, 57] and FELs [11]. In order to produce high harmonic radiation an intense femtosecond IR pulse is focused into a gas cell. A target electron absorbs several photons, recollides with its atom and thereby emits one high energetic photon. Using HHG sources, pulses in the XUV regime with durations as short as 68 as [85] can be produced. They provide excellent conditions for IR/XUV experiments: The IR pulse for the HHG is also used as probe pulse and is therefore intrinsically synchronized with the XUV pump pulse. The peak intensities achievable by HHG ($> 10^{13} \frac{\text{W}}{\text{cm}^2}$ [50]) are starting to become sufficient for XUV pump-probe experiments [45]. However the generation of these high intensities is still difficult and not yet sufficient for all systems. FELs instead routinely deliver much higher intensities up to $10^{18} \frac{\text{W}}{\text{cm}^2}$ [14] in the XUV and X-ray regime. Therefore most of the XUV pump-probe experiments are performed at FELs.

In this work XUV pump-probe experiments on two different systems, the iodine molecule I_2 and the neon dimer Ne_2 , are discussed. Our studies rely on Coulomb-explosion imaging (CEI) [74], which allows to access the molecules' geometry by exploiting the large Coulomb repulsion of the quickly ionized constituents. One XUV photon is usually sufficient to ionize an atom or molecule. At the present intensities the most likely scenario is single-photon absorption within the pump and single-photon absorption within the probe. Under these conditions mostly repulsive molecular curves are accessed at a well-defined time. These requirements justify the application of the classical model, that will be presented in the following.

The most intuitive way to simulate the measurements is by modeling molecular motion in a diatomic molecule as a classical point-like particle moving on the involved

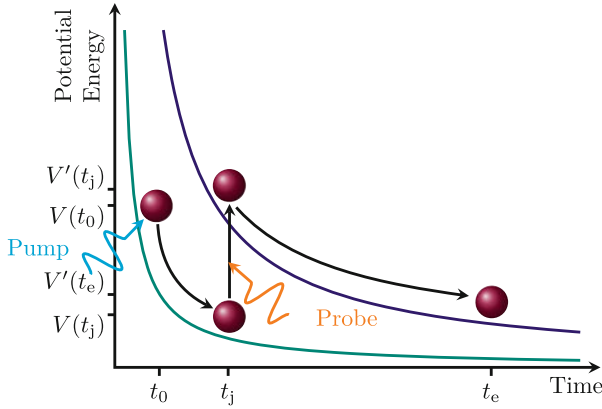


Fig. 2.10 Illustration of the classical simulation used for the present pump-probe studies. At t_0 the pump pulse prepares the classical point-like particle on the potential energy curve $V(R)$ thereby initiating dynamics in the molecule. The evolution of the system is sampled via the probe pulse at t_j by populating a different potential energy curve $V'(R)$

potential energy curves. A similar method was already successfully applied in earlier XUV pump-probe experiments [9].

According to the Franck–Condon approximation, the pump process is implemented by placing the particle on an intermediate potential curve at equilibrium internuclear distance $R(t_0) = R_{\text{eq}}$ of the neutral molecule at time t_0 , as shown in Fig. 2.10. The particle is given the reduced mass $\mu = \frac{m_1 m_2}{m_1 + m_2}$ and a vanishing initial velocity: $\frac{dR}{dt}|_{t_0=0} = 0$. In order to describe the motion of the particle, moving on the molecular potential curve $V(R)$, Newton’s classical equation of motion is solved for all internuclear distances R . The simulation is performed on an equidistant grid $(R_1, R_2, \dots, R_i, \dots, R_n)$ starting from R_{eq} with a constant step size of $\Delta R = R_i - R_{i-1}$. We start by calculating the acceleration a for each step R_i :

$$a(R_i) = -\frac{1}{\mu} \frac{V(R_i) - V(R_{i-1})}{\Delta R}. \quad (2.72)$$

The time $\Delta t(R_i - R_{i-1})$ needed to overcome ΔR with the velocity $v(R_{i-1})$ is given by

$$\Delta t(R_i - R_{i-1}) = \frac{-v(R_{i-1}) + \sqrt{v^2(R_{i-1}) + 2a(R_i)\Delta R}}{\Delta R}, \quad (2.73)$$

while the total time t_m for passing m intervals ΔR is composed of all infinitesimal intervals $t_m = \sum_{i=1}^m \Delta t(R_i - R_{i-1})$. At the end of each step the present kinetic energy of the particle is evaluated via

$$E_{\text{kin}}(R_i) = V(R_i) - V(R_{\text{eq}}), \quad (2.74)$$

in order to provide the velocity input $v(R_i)$ for the next step:

$$v(R_i) = \sqrt{\frac{2E_{\text{kin}}(R_i)}{\mu}}. \quad (2.75)$$

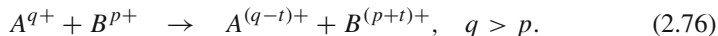
The particle pursues its motion on $V(R)$ until the probe pulse promotes it onto a different potential curve $V'(R)$ at t_j . Thus, after each step the passed time t_m must be compared with a predetermined time delay $t_D = t_j - t_0$ before starting the calculation of the trajectories. If t_m exceeds t_D the calculational procedure continues on the new potential curve $V'(R)$ with the previously gained velocity as initial condition. The transition onto a different potential energy curve is not always induced by the probe, alternatively it may occur via ICD or other decay mechanisms, as will be shown in Sect. 7.2.4.

Once the particle has reached its final potential curve, the propagation is carried on until the change in its velocity is negligible. This way the “infinite” distance $R_\infty = n\Delta R$ passed by the particle on its way to the detector is approximated. At R_∞ the total energy of the particle, gained on all populated potential curves, is evaluated. The obtained value is directly comparable to the experimentally observed kinetic energy release of the fragments (cf. Sect. 5.3.3). The used potential energy curves are either taken from literature or if not existent—which is typically the case for multiply charged molecular ions—assumed to be Coulombic.

2.7 Charge Transfer and Classical Over-the-Barrier Model

Charge transfer describes a reaction, in which electrons are transferred from one system to another. It occurs efficiently in slow ion-atom collisions, where single or multiple electrons from a typically neutral target are transferred to a highly charged projectile ion while it flies by [54]. These conditions are present in astrophysical plasmas, where charge transfer occurs between ions from solar winds and neutral clouds from comets and planetary atmospheres, leading to highly excited ions that relax via radiative decay [7]. The same effects are important for the analysis of earth-bound plasmas, as those in tokamaks [36]. Furthermore, understanding the interaction of low-energetic ions with matter plays a crucial role for heavy ion therapy [1, 43], as the deposited energy is maximal for the low projectile energies where charge transfer plays an essential role. Therefore collision experiments have explicitly addressed this question by bombarding biomolecules with low-energetic ions in order to identify the relevant break-up channels leading to DNA damage [20, 21, 76].

Here, we consider charge transfer of t electrons between the dissociating fragments B^{p+} and A^{q+} of a molecule AB :



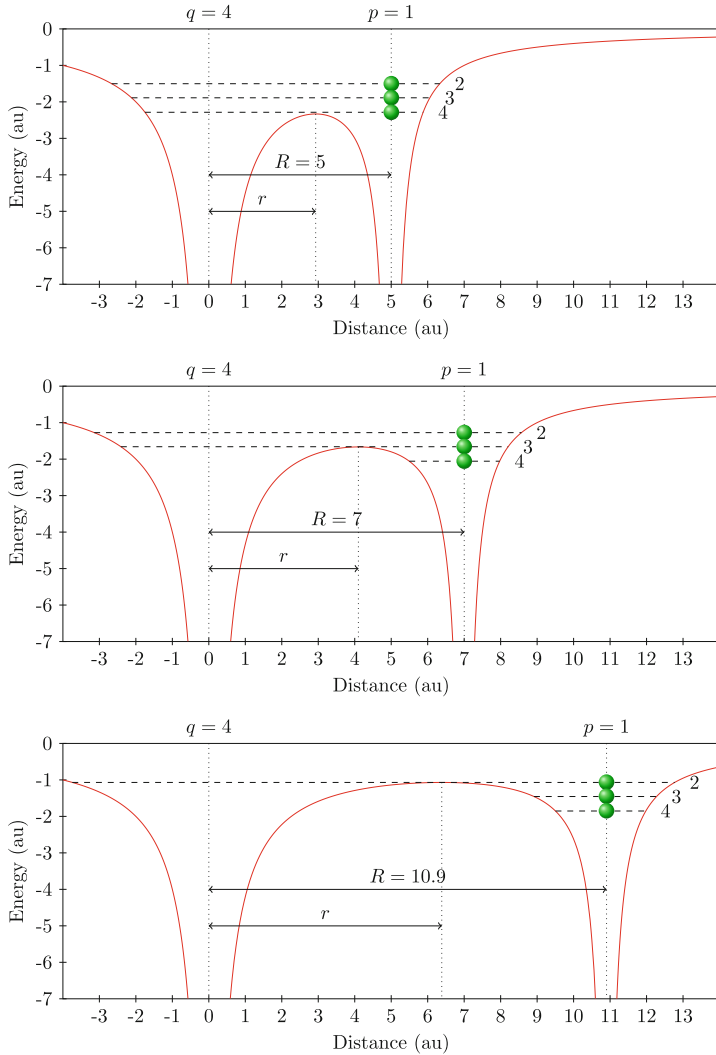


Fig. 2.11 Illustration of the over-the-barrier model for a I^{1+} and a I^{4+} ion moving apart from each other. The internuclear distance R increases from the *top* to the *bottom*. At the equilibrium internuclear distance of I_2 at 5 au the three least bound electrons may transfer to I^{4+} . Beyond 10.9 au charge transfer is not possible anymore. The required ionization potentials were taken from Table 6.2

The electrons of B^{p+} are affected by the Coulomb field of A^{q+} resulting in a lowering of the potential barrier between the two. Thus, a loosely bound electron migrates from B^{p+} to A^{q+} as soon as the potential barrier is lower than the electron's binding energy, as shown in Fig. 2.11. This process is described in the classical over-the-barrier (COB) model, first formulated in [62] and extended to state selective capture

of multiple electrons in [55]. This illustrative model and its extensions are in good agreement with experimental data and thus very popular for the description of charge transfer at low energies, like for the examples mentioned above.

The goal of the following considerations is to find an analytical expression for the critical internuclear distance R_{crit} at which charge exchange between A^{q+} and B^{p+} is not possible anymore. The binding energy $E'_i(R)$ of electron i of B^{p+} is increased in the external field of A^{q+} according to

$$E'_i(R) = -E_i - \frac{q}{R}, \quad (2.77)$$

where E_i is the binding energy experienced by the electron in the unperturbed case and R the internuclear distance. The potential $V_i(r, R)$ seen by the electron i at distance r is a superposition of the potential of its own nucleus with effective charge p_i^* and the potential of the other ion (cf. Fig. 2.11):

$$V_i(r, R) = -\left(\frac{p_i^*}{R-r} + \frac{q}{r}\right) \quad \text{for } 0 < r < R. \quad (2.78)$$

In order to determine the distance $r_{i,\text{max}}$ at which the maximum of the barrier occurs, the derivative of Eq. (2.78) is used:

$$\frac{\partial V_i(r, R)}{\partial r} = \frac{q}{r^2} - \frac{p_i^*}{(R-r)^2} \stackrel{!}{=} 0. \quad (2.79)$$

The local maximum is found by solving Eq. (2.79) for r :

$$r_{i,\text{max}} = \frac{R\sqrt{q}}{\sqrt{q} + \sqrt{p_i^*}}. \quad (2.80)$$

Upon insertion of $r_{i,\text{max}}$ into Eq. (2.78) an expression for the height of the potential barrier as a function of the internuclear distance R is found:

$$V_{i,\text{max}}(R) = -\frac{q + 2\sqrt{q} + p_i^*}{R}. \quad (2.81)$$

Since the electron i is able to overcome the potential barrier as soon as its binding energy $E'_i(R)$ is above $V_{i,\text{max}}(R)$ (cf. Fig. 2.11), Eq. (2.81) must be compared to Eq. (2.77):

$$-\frac{q}{R} + \frac{2\sqrt{q} p_i^* + p_i^*}{R} = -E_i - \frac{q}{R}, \quad (2.82)$$

This leads to

$$R_{i,\text{crit}} = \frac{2\sqrt{q} p_i^* + p_i^*}{E_i}. \quad (2.83)$$

With the help of the critical distance, the geometrical cross section for electron capture is defined as:

$$\sigma = C\pi R_{i,\text{crit}}^2 = \frac{\pi}{2} \left(\frac{2\sqrt{q p_i^*} + p_i^*}{E_i} \right)^2. \quad (2.84)$$

In order to account for the oscillatory behavior of the electron bouncing back and forth between the two ions as long as charge transfer is possible, the additional weighting factor C is introduced. Assuming that beyond $R_{i,\text{crit}}$ the electron localizes at either of the ions with equal probability, C is set⁷ to $1/2$ in Eq. (2.84).

For the purpose of this thesis extensions of the COB model [55] are not necessary since only half-collisions are considered, i.e., only the outgoing ionic fragments are observed (cf. Sect. 6.2.7).

In Fig. 2.11 the COB model is illustrated for a I^{1+} and a I^{4+} ion moving apart for various R . The effective charge p_i^* seen by electron i is assumed such that each tighter bound electron screens the nuclear charge by one. Thus, the least bound electron $i = 2$ in I^{1+} is attracted by the nucleus via the potential $-2/r$. The ionization potential of I^{1+} is taken from Table 6.2.

References

1. U. Amaldi, G. Kraft, Radiotherapy with beams of carbon ions. Rep. Prog. Phys. **68**(8), 1861 (2005)
2. V. Averbukh, L.S. Cederbaum, Calculation of interatomic decay widths of vacancy states delocalized due to inversion symmetry. J. Chem. Phys. **125**, 094107 (2006)
3. V. Averbukh et al., Interatomic electronic decay processes in singly and multiply ionized clusters. J. Electron Spectrosc. Relat. Phenom. **183**, 36 (2011)
4. L.V. Azároff (ed.), *X-ray Spectroscopy*, International Series in Pure and Applied Physics (MacGraw-Hill, New York, 1974), p. 560
5. A.P.M. Baede, *Charge Transfer between Neutrals at Hyperthermal Energies*, Advances in Chemical Physics (Wiley, Chichester, 2007), pp. 463–535
6. C.W. Bauschlicher, P.R. Taylor, Full CI benchmark calculations for molecular properties. Theoret. Chim. Acta **71**(4), 263–276 (1987)
7. P. Beiersdorfer et al., Laboratory simulation of charge exchange-produced X-ray emission from comets. Science **300**(5625), 1558–1559 (2003)
8. J.D. Bjorken, S.D. Drell, *Relativistic Quantum Mechanics*, in Sect. 7.1 (McGraw-Hill, New York, 1964)
9. I.A. Bocharova et al., Time-resolved Coulomb-explosion imaging of nuclear wavepacket dynamics induced in diatomic molecules by intense few-cycle laser pulses. Phys. Rev. A **83**, 013417 (2011)
10. R. Boge et al., Probing nonadiabatic effects in strong-field tunnel ionization. Phys. Rev. Lett. **111**, 103003 (2013)
11. R. Bonifacio, C. Pellegrini, L. Narducci, Collective instabilities and high-gain regime in a free electron laser. Opt. Commun. **50**(6), 373–378 (1984)

⁷ Comparison of measured (0.46 ± 0.05) [22] and calculated 0.452 [5] values of C shows that the assumption of $1/2$ is reasonable.

12. B.H. Boo, N. Saito, Dissociative multiple photoionization of Br₂, IBr, and I₂ in the VUV and X-ray regions: a comparative study of the inner-shell processes involving Br(3d,3p,3s) and I(4d,4p,4s,3d,3p). *J. Electron Spectrosc. Relat. Phenom.* **127**(3), 139–152 (2002)
13. M. Born, R. Oppenheimer, Zur Quantentheorie der Molekeln. *Ann. Phys.* **389**(20), 457–484 (1927)
14. J.D. Bozek, AMO instrumentation for the LCLS X-ray FEL. *Eur. Phys. J. Spec. Top.* **169**(1), 129–132 (2009)
15. C. Brechignac, J.P. Connerade, Giant resonances in free atoms and in clusters. *J. Phys. B: At. Mol. Opt. Phys.* **27**(17), 3795 (1994)
16. L.S. Cederbaum, J. Zobeley, F. Tarantelli, Giant intermolecular decay and fragmentation of clusters. *Phys. Rev. Lett.* **79**, 4778 (1997)
17. L.S. Cederbaum, *Green's Functions and Propagators for Chemistry*, Encyclopedia of Computational Chemistry (Wiley, Chichester, 2002)
18. J.P. Connerade, The non-Rydberg spectroscopy of atoms. *Contemp. Phys.* **19**(5), 415–447 (1978)
19. W. Demtröder, *Molekülphysik, theoretische Grundlagen und experimentelle Methoden*, 2 überarb. und erw. Aufl. (Oldenbourg, München, 2013), p. 487
20. Z. Deng et al., Beyond the bragg peak: hyperthermal heavy ion damage to DNA components. *Phys. Rev. Lett.* **95**, 153201 (2005)
21. Z. Deng et al., Reactive scattering damage to DNA components by hyperthermal secondary ions. *Phys. Rev. Lett.* **96**, 243203 (2006)
22. D. Dijkkamp et al., Subshell-selective electron capture in collisions of C⁴⁺, N⁵⁺, O⁶⁺ with H, H₂ and He. *J. Phys. B: At. Mol. Phys.* **18**(24), 4763 (1985)
23. F. Ehlötzky, *Quantenmechanik und Ihre Anwendungen* (Springer London, Limited, Heidelberg, 2005)
24. T. Ergler et al., Quantum-phase resolved mapping of ground-state vibrational D₂ wave packets via selective depletion in intense laser pulses. *Phys. Rev. Lett.* **97**, 103004 (2006)
25. U. Fano, Effects of configuration interaction on intensities and phase shifts. *Phys. Rev.* **124**, 1866–1878 (1961)
26. B. Fischer et al., Steering the electron in H₂⁺ by nuclear wave packet dynamics. *Phys. Rev. Lett.* **105**, 223001 (2010)
27. T. Förster, Ein Beitrag zur Theorie der Photosynthese. *Z. Naturforsch.* **2b**, 174–182 (1947)
28. T. Förster, Zwischenmolekulare Energiewanderung und Fluoreszenz. *Ann. Phys.* **437**(1–2), 55–75 (1948)
29. H. Friedrich, *Theoretical Atomic Physics*, 2nd Rev. and Enl. edn. (Springer, Berlin, 1998), p. 416
30. B.N.G. Giepmans et al., The fluorescent toolbox for assessing protein location and function. *Science* **312**(5771), 217–224 (2006)
31. D.C. Griffin, D.M. Mitnik, N.R. Badnell, Electron-impact excitation of Ne⁺. *J. Phys. B: At. Mol. Opt. Phys.* **34**(22), 4401 (2001)
32. R.E. Grisenti et al., Determination of the bond length and binding energy of the helium dimer by diffraction from a transmission grating. *Phys. Rev. Lett.* **85**, 2284–2287 (2000)
33. M. Göppert-Mayer, Über Elementarakte mit zwei Quantensprüngen. *Ann. Phys.* **401**(3), 273–294 (1931)
34. H. Haken, H.C. Wolf, *Molecular Physics and Elements of Quantum Chemistry. Introduction to Experiments and Theory*, 2nd Engl. edn. (Springer, Berlin, 2004), p. 592
35. D.R. Hartree, The calculation of atomic structures. *Rep. Prog. Phys.* **11**(1), 113 (1947)
36. M. von Hellermann et al., Investigation of thermal and slowing-down alpha particles on JET using charge-exchange spectroscopy. *Plasma Phys. Control. Fusion* **33**(14), 1805 (1991)
37. U. Hergenhahn, Interatomic and intermolecular Coulombic decay: the early years. *J. Electron Spectrosc. Relat. Phenom.* **184**, 78 (2011)
38. I.V. Hertel, C.-P. Schulz, *Atome, Moleküle und optische Physik 1. Atomphysik und Grundlagen der Spektroskopie* (Springer, Berlin, 2008)

39. I.V. Hertel, C.-P. Schulz, *Atome, Moleküle und optische Physik 2. Moleküle und Photonen - Spektroskopie und Streuphysik* (Springer, Berlin, 2010), p. 639
40. T. Jahnke et al., Experimental observation of interatomic Coulombic decay in neon dimers. *Phys. Rev. Lett.* **93**, 163401 (2004)
41. J.E. Jones, On the determination of molecular fields. II. From the equation of state of a gas. *Proc. R. Soc. Lond. Ser. A* **106**(738), 463–477 (1924)
42. L. Keldysh, Ionization in the field of a strong electromagnetic wave. *Sov. Phys. JETP* **20**(5), 1307–1314 (1965)
43. G. Kraft, M. Scholz, U. Bechthold, Tumor therapy and track structure. *Radiat. Environ. Biophys.* **38**(4), 229–237 (1999)
44. M. Kurka, Zwei-Photonen-Doppelionisation von Helium und D₂-Molekülen am Freie-Elektronen-Laser in Hamburg. Ph.D. thesis, Heidelberg, 2011
45. D.E. Laban et al., Extreme ultraviolet interferometer using high-order harmonic generation from successive sources. *Phys. Rev. Lett.* **109**, 263902 (2012)
46. I.N. Levine, *Quantum Chemistry*, 7th edn. Pearson Advanced Chemistry Series, Internat. edn. (Pearson, Boston, 2014), p. 700 (erschienen 2013)
47. M. Lewenstein et al., Theory of high-harmonic generation by low-frequency laser fields. *Phys. Rev. A* **49**, 2117–2132 (1994)
48. H.H. Madden, Chemical information from Auger electron spectroscopy. *J. Vac. Sci. Technol.* **18**(3), 677–689 (1981)
49. S. Marburger et al., Experimental evidence for interatomic Coulombic decay in Ne clusters. *Phys. Rev. Lett.* **90**, 203401 (2003)
50. H. Mashiko, A. Suda, K. Midorikawa, Focusing multiple high-order harmonics in the extreme-ultraviolet and soft-X-ray regions by a platinum-coated ellipsoidal mirror. *Appl. Opt.* **45**(3), 573–577 (2006)
51. L. Meitner, Über die Beta-Strahl-Spektren und ihren Zusammenhang mit der Gamma-Strahlung. *Z. Phys.* **11**(1), 35–54 (1922)
52. E. Mevel et al., Atoms in strong optical fields: evolution from multiphoton to tunnel ionization. *Phys. Rev. Lett.* **70**, 406–409 (1993)
53. P.M. Morse, Diatomic molecules according to the wave mechanics. II. Vibrational levels. *Phys. Rev.* **34**, 57–64 (1929)
54. A. Müller, E. Salzborn, Scaling of cross sections for multiple electron transfer to highly charged ions colliding with atoms and molecules. *Phys. Lett. A* **62**(6), 391–394 (1977)
55. A. Niehaus, A classical model for multiple-electron capture in slow collisions of highly charged ions with atoms. *J. Phys. B: At. Mol. Phys.* **19**(18), 2925 (1986)
56. G. Parisi, *Statistical Field Theory*. Frontiers in Physics, vol. 66 (Addison-Wesley, Redwood City, 1988), p. 352
57. P.M. Paul et al., Observation of a train of attosecond pulses from high harmonic generation. *Science* **292**(5522), 1689–1692 (2001)
58. F. Penning, Über Ionisation durch metastabile Atome. *Naturwissenschaften* **15**(40), 818–818 (1927)
59. E.A. Power, S. Zienau, Coulomb gauge in non-relativistic quantum electro-dynamics and the shape of spectral lines. *Philos. Trans. R. Soc. Lond. A Math. Phys. Sci.* **251**(999), 427–454 (1959)
60. U.V. Riss, H.D. Meyer, Calculation of resonance energies and widths using the complex absorbing potential method. *J. Phys. B: At. Mol. Opt. Phys.* **26**(23), 4503 (1993)
61. B.O. Roos, *The Complete Active Space Self-Consistent Field Method and Its Applications in Electronic Structure Calculations*, Advances in Chemical Physics (Wiley, Chichester, 2007), pp. 399–445
62. H. Ryufuku, K. Sasaki, T. Watanabe, Oscillatory behavior of charge transfer cross sections as a function of the charge of projectiles in low-energy collisions. *Phys. Rev. A* **21**, 745–750 (1980)
63. R. Santra, L.S. Cederbaum, An efficient combination of computational techniques for investigating electronic resonance states in molecules. *J. Chem. Phys.* **115**, 6853 (2001)

64. R. Santra, J. Zobeley, L.S. Cederbaum, Electronic decay of valence holes in clusters and condensed matter. *Phys. Rev. B* **64**, 245104 (2001)
65. R. Santra et al., Interatomic Coulombic decay in van der Waals clusters and impact of nuclear motion. *Phys. Rev. Lett.* **85**, 4490 (2000)
66. R. Santra, L.S. Cederbaum, Non-Hermitian electronic theory and applications to clusters. *Phys. Rep.* **368**(1), 1–117 (2002)
67. S. Scheit, L.S. Cederbaum, H.-D. Meyer, Time-dependent interplay between electron emission and fragmentation in the interatomic Coulombic decay. *J. Chem. Phys.* **118**, 2092 (2003)
68. S. Scheit et al., On the interatomic Coulombic decay in the Ne dimer. *J. Chem. Phys.* **121**, 8393 (2004)
69. J. Schirmer, L.S. Cederbaum, O. Walter, New approach to the one-particle Green's function for finite Fermi systems. *Phys. Rev. A* **28**, 1237–1259 (1983)
70. C.D. Sherrill, H.F. Schaefer III, in *The Configuration Interaction Method: Advances in Highly Correlated Approaches*, ed. by M.C.Z. Per-Olov Löwdin, J.R. Sabin, E. Brändas. *Advances in Quantum Chemistry*, vol. 34 (Academic Press, New York, 1999), pp. 143–269
71. A.J.F. Siegert, On the derivation of the dispersion formula for nuclear reactions. *Phys. Rev.* **56**, 750–752 (1939)
72. B.M. Smirnov, Ionization in low-energy atomic collisions. *Phys. Usp.* **24**(4), 251–275 (1981)
73. J. Tremblay et al., Photoelectron spectroscopy of atomic iodine produced by laser photodissociation. *Phys. Rev. A* **38**, 3804–3807 (1988)
74. Z. Vager, R. Naaman, E.P. Kanter, Coulomb explosion imaging of small molecules. *Science* **244**(4903), 426–431 (1989)
75. N. Vaval, L.S. Cederbaum, Ab initio lifetimes in the interatomic Coulombic decay of neon clusters computed with propagators. *J. Chem. Phys.* **126**, 164110 (2007)
76. J. de Vries et al., Charge driven fragmentation of nucleobases. *Phys. Rev. Lett.* **91**, 053401 (2003)
77. V. Weisskopf, E. Wigner, Berechnung der natürlichen Linienbreite auf Grund der Diracschen Lichttheorie. *Z. Phys.* **63**(1–2), 54–73 (1930)
78. H. Werner, P.J. Knowles, An efficient internally contracted multiconfiguration-reference configuration interaction method. *J. Chem. Phys.* **89**(9), 5803–5814 (1988)
79. Wikimedia Commons [GFDL or CC-BY-SA-3.0-2.5-2.0-1.0], Electromagnetic Spectrum (2011)
80. Wikimedia Commons [GFDL or CC-BY-SA-3.0-migrated], EM Spectrum Properties (2007)
81. Wikimedia Commons [Public Domain], Franck-Condon-Prinzip (2007)
82. R.G. Woolley, Molecular quantum electrodynamics. *Proc. R. Soc. Lond. A Math. Phys. Sci.* **321**(1547), 557–572 (1971)
83. J. Yeh, I. Lindau, Atomic subshell photoionization cross sections and asymmetry parameters: $1 \leq Z \leq 103$. *At. Data Nucl. Data Tables* **32**(1), 1–155 (1985)
84. A.H. Zewail, Femtochemistry: atomic-scale dynamics of the chemical bond using ultrafast lasers (Nobel lecture). *Angew. Chem. Int. Ed.* **39**(15), 2586–2631 (2000)
85. K. Zhao et al., Tailoring a 67 attosecond pulse through advantageous phasemismatch. *Opt. Lett.* **37**(18), 3891–3893 (2012)
86. J. Zobeley, Elektronische Relaxationsprozesse Inner-Valenz-ionisierter Moleküle und Cluster. Ph.D. thesis, Heidelberg, 2005

XUV Pump-Probe Experiments on Diatomic Molecules
Tracing the Dynamics of Electron Rearrangement and
Interatomic Coulombic Decay

Schnorr, K.

2015, XI, 191 p. 95 illus., 25 illus. in color., Hardcover

ISBN: 978-3-319-12138-3